

UNCLASSIFIED

AD NUMBER
AD482662
NEW LIMITATION CHANGE
TO Approved for public release, distribution unlimited
FROM Distribution authorized to U.S. Gov't. agencies and their contractors; Critical Technology; MAY 1966. Other requests shall be referred to Air For Weapons Laboratory, ATTN: WLRP, Kirtland AFB, NM 87117.
AUTHORITY
AFWL ltr dtd 30 Nov 1971

THIS PAGE IS UNCLASSIFIED

✓
AFWL-TR-66-13 ✓

20
3-7
AFWL TR
66-13

ATTENUATION OF SHOCK WAVES IN DISTENDED MATERIALS

Ronald K. Linde
David N. Schmidt

Stanford Research Institute ✓
Menlo Park, California
Contract AF29(601)-6734 *Hand*

TECHNICAL REPORT NO. AFWL-TR-66-13

May 1966

AIR FORCE WEAPONS LABORATORY
Research and Technology Division
Air Force Systems Command
Kirtland Air Force Base
New Mexico



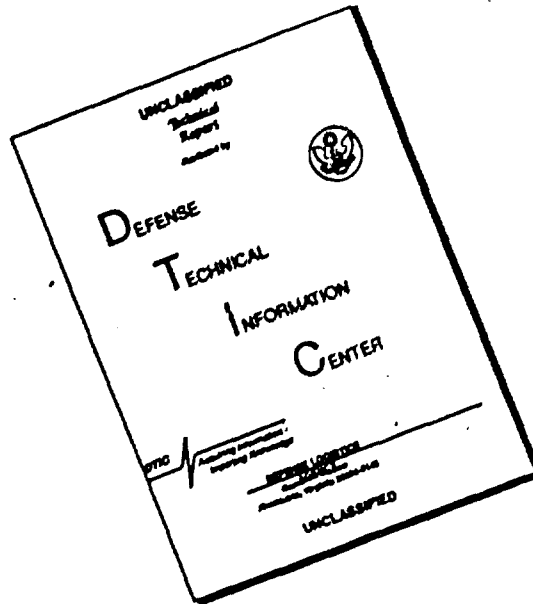
482662



D D C

D D C

DISCLAIMER NOTICE



THIS DOCUMENT IS BEST QUALITY AVAILABLE. THE COPY FURNISHED TO DTIC CONTAINED A SIGNIFICANT NUMBER OF PAGES WHICH DO NOT REPRODUCE LEGIBLY.

AFWL-TR-66-13

Research and Technology Division
AIR FORCE WEAPONS LABORATORY
Air Force Systems Command
Kirtland Air Force Base
New Mexico

When U. S. Government drawings, specifications, or other data are used for any purpose other than a definitely related Government procurement operation, the Government thereby incurs no responsibility nor any obligation whatsoever, and the fact that the Government may have formulated, furnished, or in any way supplied the said drawings, specifications, or other data, is not to be regarded by implication or otherwise, as in any manner licensing the holder or any other person or corporation, or conveying any rights or permission to manufacture, use, or sell any patented invention that may in any way be related thereto.

This report is made available for study with the understanding that proprietary interests in and relating thereto will not be impaired. In case of apparent conflict or any other questions between the Government's rights and those of others, notify the Judge Advocate, Air Force Systems Command, Andrews Air Force Base, Washington, D. C. 20331.

This document is subject to special export controls and each transmittal to foreign governments or foreign nationals may be made only with prior approval of AFWL (WLRP), Kirtland AFB, N. M. 87117. Distribution is limited because of the technology discussed in this report.

COLLECTION NO.	
FORM	WRITE SECTION
NO.	DATE RECEIVED
JUSTIFICATION	
BY	
DATE DUTY/AVAILABILITY ORDER	
DIST.	ATL. TR. SPECIAL
2	

(18) AFWL TR-66-13 (19)

(6) ATTENUATION OF SHOCK WAVES IN DISTENDED MATERIALS.

(10) Ronald K. Linde
David N. Schmidt.

(9) Final rept. 15 Jan 65-2 Mar 66,

Stanford Research Institute
Menlo Park, California

Contract AF29(601)-6734

(15) 7-
(16) AF-5710, SFI-GSU-5286

TECHNICAL REPORT NO. AFWL-TR-66-13

(11) May 66,

(12) 104 p.

This document is subject to special export controls and each transmittal to foreign governments or foreign nationals may be made only with prior approval of AFWL (WLRP), Kirtland AFB, N.M. Distribution of this document is limited because of the technology discussed.

(332500)

1475
wh

FOREWORD

This report was prepared by the Stanford Research Institute, Menlo Park, California, under Contract AF29(601)-6734. The research was performed under Program Element 7.60.06.01.D, Project 5710, Subtask 15.018, and was funded by the Defense Atomic Support Agency (DASA).

Inclusive dates of research were 18 January 1965 through 2 March 1966. The report was submitted 6 April 1966 by the AFWL Project Officer, Capt George P. Crotwell, Jr., (WLRP). The Contractor's report number is SRI Project GSU-5386. ^{it}

The authors wish to thank the many people who have made significant contributions to the work reported herein. Included are Capt G.P. Crotwell (Project Officer), G. R. Fowles (project supervisor), A. C. Wheeler (mechanical design and assembly), P. S. DeCarli (material fabrication and metallography), G. E. Duvall and B. B. Wheeler (computer program), W. J. Murri, A. J. Hunt, and M. M. Grathwol (data reduction and analysis), L. B. Hall and A. J. Bartlett (dynamic measurements), and B. O. Reese (static compression measurements).

This report has been reviewed and is approved.



GEORGE P. CROTWELL, JR.
Captain USAF
Project Officer



CYDE C. REYNOLDS
Lt Colonel USAF
Chief, Physics Branch



WILLIAM E. STEPHENS
Colonel USAF
Chief, Research Division

ABSTRACT

Porous graphite and specially prepared aluminum foams (40 to 80 percent of crystal density) were investigated in an attempt to deduce the effect of such material parameters as particle (or pore) shape, size, and size distribution on response of the materials to shock loading. Results suggest that the strength of the solid matrix and the porosity are more important than particle geometry per se.

Hugoniot's for one aluminum and one graphite foam (both about three-fourths of crystal density) were measured in detail up to about 25 kbar. In the pressure and porosity range studied, the P-V Hugoniot's of the foams after compaction have been found to be very close to those of the solid materials. Recovered shocked specimens of aluminum foam exhibited densities characteristic of solid aluminum, whereas recovered shocked specimens of ATJ graphite had densities very close to their initial densities.

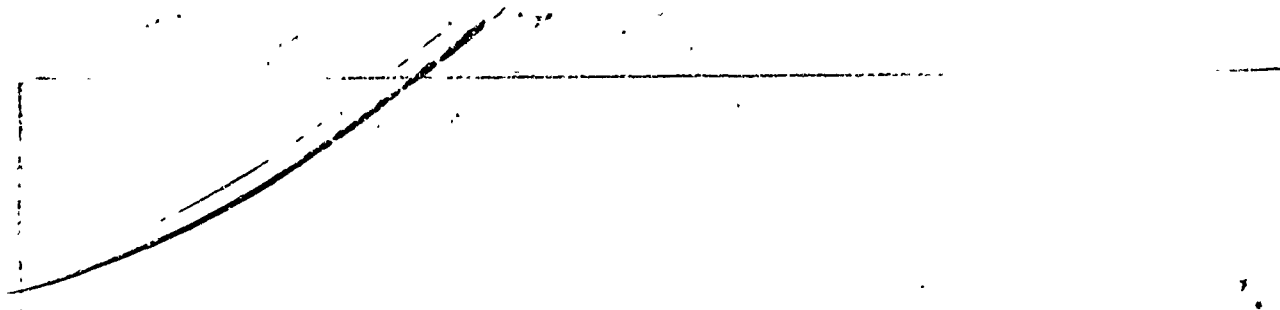
An artificial viscosity digital computer code was adapted to foams and shown to be capable of predicting approximate shock attenuation behavior of porous solids as measured experimentally.

AFWL-1B-66-15

This page intentionally left blank.

CONTENTS

<u>Section</u>		<u>Page</u>
I	INTRODUCTION	1
II	THEORETICAL BACKGROUND	3
III	SHOCK ATTENUATION CALCULATIONS	11
	1. Description of Method	11
	2. Equations of State	12
IV	MATERIAL DEVELOPMENT	19
	1. Specimen Fabrication	19
	2. Metallography and Quality Control	21
V	EXPERIMENTAL TECHNIQUES	25
	1. Shock Wave Measurements	25
	2. Measurement of Longitudinal Sound Velocities	43
VI	EXPERIMENTAL RESULTS AND DISCUSSION	47
	1. Parameter Variation	47
	2. Terminal Observations on Recovered Material	48
	3. Hugoniot of Foams	52
	4. Shock Attenuation Experiments and Calculations	59
VII	SUMMARY AND RECOMMENDATIONS FOR FURTHER WORK	67
<u>Appendices</u>		
I	DESCRIPTION OF CALCULATION ROUTINE USING THE ARTIFICIAL VISCOSITY CODE	71
II	MATERIAL DESIGNATIONS AND SUPPLIERS	85
III	TABULATED SUMMARY OF STATIC AND DYNAMIC DATA	87
REFERENCES		97
DISTRIBUTION		98



ILLUSTRATIONS

<u>Figure</u>		<u>Page</u>
1	Hugoniot for Elastic Locking Solid	4
2	Possible Hugoniots for Porous Solids	6
3	Assumed P-V Diagram in PHASETRANSITION Procedure	14
4	Assumed P-V Diagram in NOREL Procedure	17
5	Powders Used for Making Sintered Aluminum Foam	23
6	Typical Aluminum Foam Types	24
7	Illustration of Impedance-Match Method for Measuring Target Hugoniot	25
8	Illustration of Procedure for Hugoniot Measurement when a Double Wave Structure Exists	27
9	Calibration Curve for Quartz Gage with $A = 0.201 \text{ in.}^2$, $l = 0.376 \text{ in.}$, and $R = 51.0 \Omega$	29
10	Target Configuration Immediately prior to Impact	31
11	Configuration of Gas Gun prior to Target Alignment	32
12	Projectile Assembly for Shock Attenuation Studies	35
13	Binary Coder Circuit for Distinguishing Electrical Pin Closures	38
14	Oscilloscope Records Showing Tilt-Pin Closures and Cathode Modulation Time Marks	39
15	Block Diagram of Instrumentation for Recording and Calibrating Data Signals	41
16	(a) Calibration Record for Cathode Modulation Timing System	
	(b) Quartz Gage Record with Cathode Modulation Time Marks (Shot 11, 659)	42
17	Block Diagram of System for Measurement of Longitudinal Sound Velocity	44

ILLUSTRATIONS (Concluded)

<u>Figure</u>		<u>Page</u>
18	Pressure, Particle-Velocity Diagram for 2.1 g/cm ³ "Chunk" Aluminum Foam	53
19	Pressure-Particle Velocity Diagram for Various Aluminum Foams	54
20	Pressure, Particle-Velocity Diagram for Graphite and Carbon Foams	55
21	Typical Voltage-Time Profiles from Quartz	56
22	Reconstructed and Computed Pressure-Time Profiles at Foam-Quartz Interface for Shock Attenuation Studies	62
23	Reconstructed and Computed Pressure-Time Profiles at Foam-Quartz Interface for Shock Attenuation Studies	63
24	Reconstructed and Computed Pressure-Time Profiles at Foam-Quartz Interface, Showing Effect of Variations in Computational Procedure	64
25	Flow Chart for NOREL Procedure	77

TABLES

<u>Table</u>		<u>Page</u>
I	Density Data for Recovered Shocked Foams	50
II	Residual Densities of Quasi-Statically Compressed Foams	51
III	Values of Quantities Used in Drawing Smooth Curves of Figs. 13 to 20	57
IV	Data for Shock Attenuation Experiments	60
V	Measured Longitudinal Acoustic Velocities	89
VI	Summary of Graphite and Carbon Data from Quartz Gage Shots	90
VII	Summary of Aluminum Data from Quartz Gage Shots	92
VIII	Summary of Static Compression Data for Carbon and Graphite Specimens	94
IX	Summary of Static Compression Data for Aluminum Specimens	95

SECTION I

INTRODUCTION

Research on foams (distended solids) was undertaken at Poulter Laboratories in 1962¹ because it was recognized that such highly compressible materials should be effective in reducing the peak pressure delivered to a solid boundary by a given impulse at the opposite surface of the foam material. Since that time work on representatives of several classes of distended materials, including plastics, metals, ceramics, and graphite, has been performed at Poulter Laboratories under U. S. Air Force Weapons Laboratory sponsorship.^{1, 2, 3}

Although all the foams previously studied have shown similar behavior in a gross sense, there are important differences in their relative effectiveness as countermeasure materials. The current program of research was therefore undertaken to study two types of foam (aluminum and graphite) in detail in an attempt to (1) discover the effect of varying individual material parameters, (2) investigate the nature of foam Hugoniot,* and (3) study shock attenuation in the foams as a basis for comparison with theoretical predictions.

* As used in this report the term "Hugoniot" is applied to foams to mean the locus of final macroscopic pressure-volume or pressure-particle velocity states of shocked material deduced from experimental observations and invocation of the so-called "jump" conditions.

AFWL-TR-66-13

This page intentionally left blank.

SECTION II

THEORETICAL BACKGROUND

The Hugoniot equation of state of foams is often approximated by the elastic locking-solid model, which is represented in the pressure-volume plane in Fig. 1. For this model, the material behaves like an isotropic elastic solid below a certain critical pressure P_e . Above the critical elastic wave amplitude associated with the point (P_e, V_e) , the pore space collapses irreversibly, and the material locks at volume V_1 , so that it behaves like an incompressible solid by comparison with the porous material. For the limiting case of a simple locking solid, $P_e = 0$ and $V_e = V_0$. In reality, the precise shape of the horizontal portion of the schematic Hugoniot of Fig. 1 would be expected to depend upon the particular foam material in question, but should ideally be a shallow, rising curve with positive curvature.

In practice, if calculations of shock interaction or attenuation are to be made, the vertical portion of the curve is often replaced with the Hugoniot of the solid material from which the matrix of the foam was constructed. Although it is impossible (on thermodynamic grounds) for specimens of different porosity to have Hugoniots which exactly coincide in a region of the pressure-volume plane, it may in practice be a very good approximation for a given matrix material over a certain range of porosities and shock pressures, as is demonstrated by the experimental results discussed in this report.

Let us consider a shock traveling through material initially in a state characterized by pressure P_0 , specific volume V_0 , and total internal energy E_0 .

Now if

$$E = E(P, V)$$

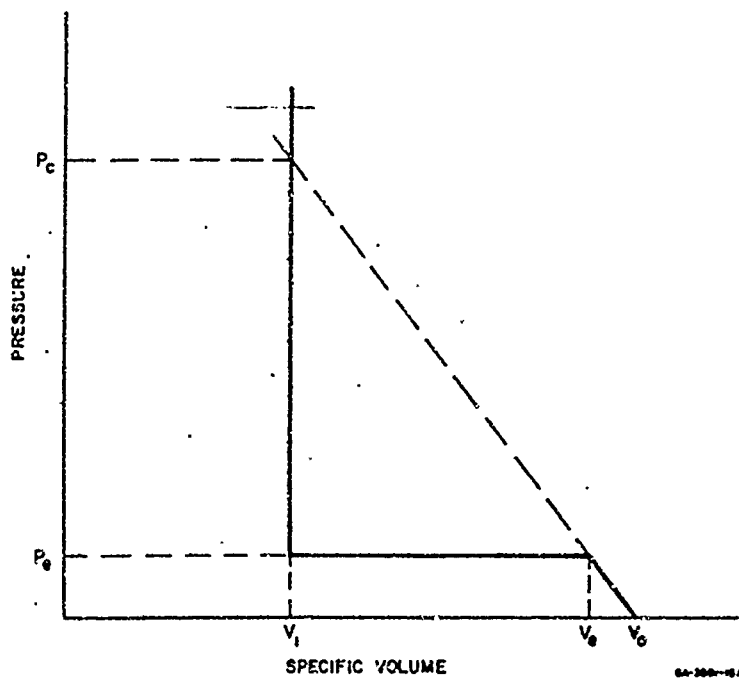


FIG. 1 HUGONIOT FOR ELASTIC LOCKING SOLID

therefore

$$dE = \left(\frac{\partial E}{\partial V} \right)_P dV + \left(\frac{\partial E}{\partial P} \right)_V dP \quad (1)$$

But conservation of energy across the shock front leads to

$$E - E_0 = \frac{1}{2}(P + P_0)(V_0 - V)$$

so that

$$dE = -\frac{1}{2}(P + P_0)dV + \frac{1}{2}(V_0 - V)dP \quad (2)$$

Thus

$$\frac{dP}{dV} = \frac{\frac{1}{2}(P + P_0) + \left(\frac{\partial E}{\partial V} \right)_P}{\frac{1}{2}(V_0 - V) - \left(\frac{\partial E}{\partial P} \right)_V} \quad (3)$$

But if thermal equilibrium is assumed (as an approximation), we have $(\partial E/\partial P)_V = V/\Gamma$, where Γ is the so-called Grüneisen coefficient; and

$$\left(\frac{\partial E}{\partial V}\right)_P = \frac{C_P - P\left(\frac{\partial V}{\partial T}\right)_P}{\left(\frac{\partial V}{\partial T}\right)_P} = \frac{C_P}{V\alpha} - P \quad (4)$$

where C_P is the heat capacity at constant pressure and α is the coefficient of thermal expansion. Therefore

$$\frac{dP}{dV} = \frac{\frac{2C}{V\alpha}P + P_0 - P}{V_0 - \left(1 + \frac{2}{\Gamma}\right)V} \quad (5)$$

Thus, in general, the slope dP/dV becomes infinite when $V_0/V = 1 + 2/\Gamma$ and becomes positive when $V_0/V > 1 + 2/\Gamma$, so that the limiting compression is equal to $1 + 2/\Gamma$ unless the material has an unusual equation of state or a first-order phase transition occurs. In other words, if we have a porous solid with $V_0 > V_s$, where V_s is the initial specific volume of nonporous material, then the limiting compacted volume will be greater than the limiting volume for initially nonporous material. In fact, if $V_0/V_s > 1 + 2/\Gamma$ the Hugoniot would be expected to have positive slope, since a small pressure $P > P_e$ should compact the foam to very nearly solid density but a strong shock can compact it no more than to a volume of $V_0/(1 + 2/\Gamma)$. If $V_0/V_s = 1 + 2/\Gamma$ we have in principle the vertical Hugoniot associated with the ideal locking solid. For $V_0/V_s < 1 + 2/\Gamma$ we have above P_e the more familiar Hugoniot shape commonly associated with the shock compression of initially solid materials. These cases are illustrated schematically in Fig. 2.

For purposes of illustration let us explore a specific case. A commonly used equation of state (Mie-Grüneisen) for solids takes the

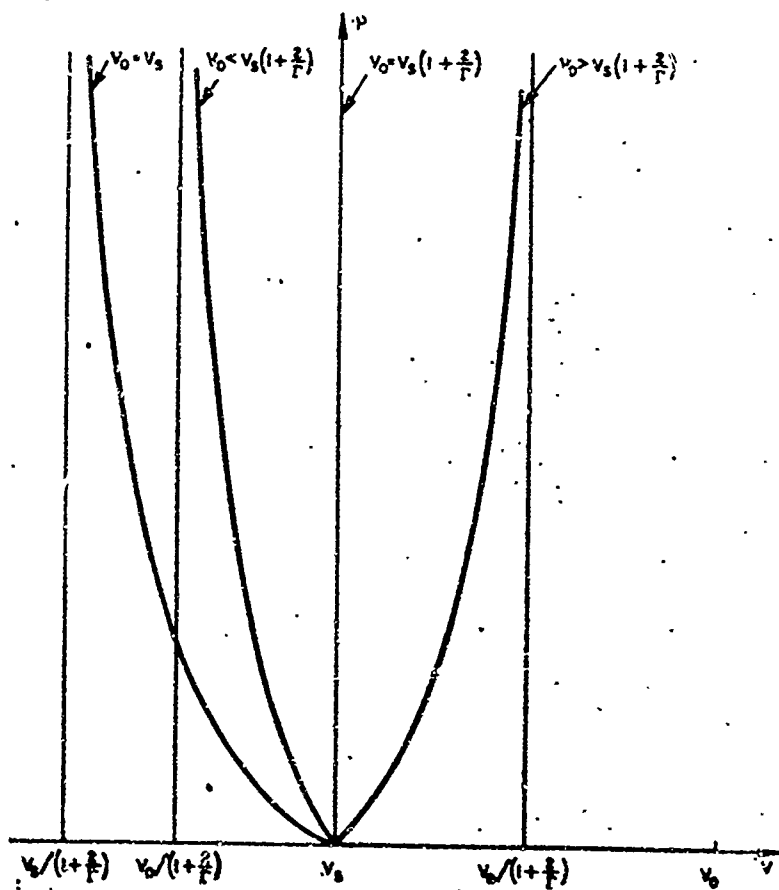


FIG. 2 POSSIBLE HUGONIOTS FOR POROUS SOLIDS
 For simplicity, P_0 has been set equal to zero

form

$$P = - \frac{\partial E_c}{\partial V} + A \frac{T}{V} \quad (6)$$

where E_c is the internal energy of material compressed to volume V at a temperature of $0^\circ K$ (i.e., E_c is the "compressional part" of the total internal energy E); P is the pressure at volume V and temperature T ; and A is an undetermined coefficient. Now if for simplicity the heat capacity at constant volume C_v is assumed not to vary with T , then $E = E_c + C_v T$, and we have

$$P + \frac{\partial E_c}{\partial V} = \Gamma \frac{E - E_c}{V} \quad (7)$$

where $\Gamma = A/C_v = V(\partial P/\partial E)_V$ is the Grüneisen coefficient.

Using the conservation of energy relation

$$E - E_0 = \frac{1}{2}(P_0 + P)(V_0 - V)$$

with E_0 and P_0 set arbitrarily to zero yields

$$V \frac{\partial E_c}{\partial V} + \Gamma E_c = -\Gamma \frac{PV}{2} \left(1 + \frac{2}{\Gamma} - \frac{V_0}{V} \right) \quad (8)$$

along the Hugoniot, so that

$$P = - \frac{V \frac{\partial E_c}{\partial V} + \Gamma E_c}{\frac{\Gamma V}{2} \left(1 + \frac{2}{\Gamma} - \frac{V_0}{V} \right)} \quad (9)$$

Now,

$$\Gamma = V \left(\frac{\partial P}{\partial E} \right)_V = V \frac{\alpha}{C_p K + T\alpha^2} = - \frac{V\alpha}{KC_v} \quad (10)$$

where $\alpha = (\partial V/\partial T)_P/V$ is the coefficient of thermal expansion and $K = (\partial V/\partial P)_T/V$ is the bulk isothermal compressibility. At room temperature and atmospheric pressure, this yields $\Gamma \approx 2.1$ for aluminum.

For solids, Γ will generally fall between 1 and 4. Thus, the critical distention for "cross-over" of the Hugoniot should be somewhere between $V_0/V_s = 1.5$ and $V_0/V_s = 3$. As the pressure increases, V_0/V approaches the limiting value $1+2/\Gamma$. Therefore, the limiting value of V is proportional to the initial specific volume V_0 , provided that Γ remains constant (as it should for the pressure range considered in this report). In actuality, Γ may be expected to decrease with decreasing volume and with increasing temperature, but should still be on the order of 1 to 2 even at very high pressure.

The theoretical basis for foams serving as effective pressure attenuators is covered in detail in Reference 1 and will be only qualitatively summarized here. Foams are effective as countermeasure materials because, first of all, a Hugoniot which resembles that of Fig. 1 implies a large ratio of rarefaction velocity to shock velocity. A shock front travels at a velocity proportional to the square root of the slope of the straight line connecting the initial and the shocked states in the P-V plane. The sum of the particle velocity and longitudinal sound velocity in the compressed material behind the shock is proportional to the square root of the slope of the adiabat through the shocked state. The first means of attenuation may be thought of as caused by rarefactions overtaking the shock pulse from the rear. Therefore, foams are especially effective because they provide a large rarefaction-to-compaction velocity ratio (see Fig. 1). Alternative ways of looking at the same effect in terms of energy dissipation or of "momentum spreading" lead to the same conclusions.

A very important advantage can be gained by the presence of a forerunner wave. For shock pressures between certain limits (i. e., between P_0 and P_c in Fig. 1), the shock front splits up into two waves, the first of these waves having amplitude P_0 . Since momentum and energy must be conserved, attenuation of the second (slower) wave will

be enhanced as the amount of material included between the two wavefronts increases. The rate of attenuation will also be proportional to the momentum per unit volume of this included material. Thus, it is desirable to have the velocity difference between the waves as high as possible and to have the value of P_e as large as possible, provided that the critical damage pressure in the structure to be protected will not be exceeded when the forerunner wave reaches the structure-foam interface.

AFW-TR-66-13

This page intentionally left blank.

SECTION III

SHOCK ATTENUATION CALCULATIONS

1. Description of Method

Calculations of shock propagation and interaction may be made precisely using the method of characteristics; however, this method soon becomes unwieldy when used for any but the simplest problems and is difficult to organize into a digital computer code. As an alternative, the artificial viscosity method (Q-method) of von Neumann and Richtmyer⁶ is readily adapted to computer calculations but has the possible disadvantage of spreading the shock front over a finite distance. The Q-method uses finite difference equations in real space and time to represent differential equations describing the flow.^{6, 7} The artificial viscosity Q is added to the pressure in the difference equations to remove all discontinuities in the flow.

The Q-method has been used for all shock attenuation calculations reported here.

The value of Q used was given by

$$Q = -\Delta u \left[C_q^2 |\Delta u| + C_{ona} C_{sp} \right] / V \quad (11)$$

where C_q and C_{ona} are arbitrary constants which were set equal to 2.0 and 0.1, respectively; C_{sp} is the local acoustic velocity, V is the local specific volume, and Δu is the particle velocity increment (i.e., local particle speed difference between adjacent cells of constant mass). It should be noted that Q as given above has a negligible value outside the shock region.

The computations were carried out on a Burroughs B5500 digital computer from an ALCOL program developed by John O. Erkman and

adapted to porous solids by George Duvall. The essential steps in the calculation are summarized in Appendix I, where the entire program has also been reproduced.

2. Equations of State

The equation of state information has been programmed as follows:

2 lb/ft³ Styrofoam

The relations

$$P = P_2 \left[\frac{V_1 - V}{V_1 - V_2} + b \frac{(V - V_1)(V - V_2)}{(V_1 - V_2)^2} \right] \quad (12)$$

$$\text{for } \begin{cases} V_2 < V < V_1 \\ 0 < P < P_2 \end{cases}$$

where $P_2 = 1.0$ kbar, $V_1 = 31.25$ cm³/g, $V_2 = 0.9422$ cm³/g, and $b = 0.1$; and

$$P = A \left(\frac{V_G}{V} - 1 \right) + B \left(\frac{V_G}{V} - 1 \right)^2 \quad (13)$$

$$\text{for } \begin{cases} V < V_G \\ P < P_2 \end{cases}$$

where $A = 90.5$ kbar, $B = 200$ kbar, and $V_G = 0.9524$ cm³/g, (based on the data of Wagner et al.⁸ for 1.05 g/cm³ polystyrene) have been used in the STYROFOAM procedure (see Appendix I).

6061-T6 Aluminium Flyer Plate

The relations

$$P = 1044 \left(\frac{V_0 - V}{V_0} \right) \text{ for } 0 \leq P \leq 6.4 \text{ kbar}$$

and

$$P = 794 \left(\frac{V_0 - V}{V_0} \right) + 1.6 \text{ for } 6.4 < P \leq 31 \text{ kbar} \quad (14)$$

have been given by Lundergan and Herrmann⁹ and were adapted to the elastoplastic model using the ELASTOPLASTIC procedure developed by Erkman¹⁰ (see Appendix I).

Quartz

The relation

$$P = 869.5 (1 - V/V_0) \text{ kbar}, \quad (15)$$

where $V_0 = 3.774 \text{ cm}^3/\text{g}$, has been devised from the data of Graham et al.¹¹ and used in the WATER procedure (see Appendix I) to represent the equation of state of quartz under both shock and rarefaction. The value $0.5728 \text{ cm}/\mu\text{sec}$ has been used for C_{sp} of Eq. (11).

Porous Targets

For the porous aluminum and graphite targets a new procedure called PHASETRANSITION which allows hysteresis to exist in a compression-rarefaction cycle has been written by George Duvail. The available P-V information for the porous targets and the assumptions made here are best described with reference to Fig. 3.

The experimental results reported in Section VI give values for the amplitude P_1 of the forerunner wave in the target material and for the corresponding specific volume V_1 . These, with the initial volume V_0 , give the end points of a quadratic which has negative slope and positive curvature for $V_1 \leq V \leq V_0$, provided that $0 < b \leq 1$:

Along AB

$$P = f_1(V) = P_1 \left[\frac{(V-V_0)}{V_1-V_0} + b \frac{(V-V_0)(V-V_1)}{(V_1-V_0)^2} \right] \quad (16)$$

where $V_0 = 0.478 \text{ cm}^3/\text{g}$, $V_1 = 0.474 \text{ cm}^3/\text{g}$, $P_1 = 0.446 \text{ kbar}$ and $b = 0.1$ for the 2.1 g/cm^3 aluminum foam studied and $V_0 = 0.580 \text{ cm}^3/\text{g}$, $V_1 = 0.576 \text{ cm}^3/\text{g}$, $P_1 = 0.27 \text{ kbar}$, $b = 0.1$ for the ATJ graphite.

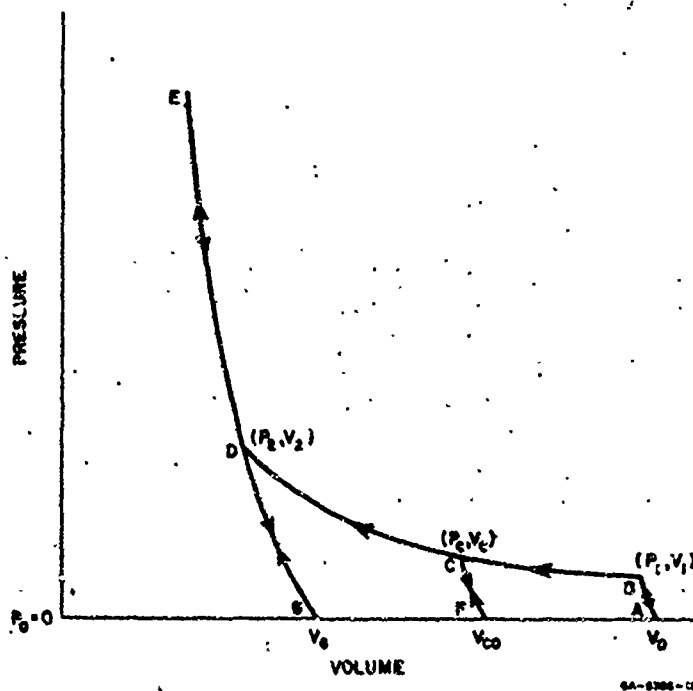


FIG. 3 ASSUMED P-V DIAGRAM IN PHASE TRANSITION PROCEDURE

The quadratic form for the P-V curve in this region was chosen for the following reason: If a wavefront is stable, the locus of states in the P-V plane followed by a mass element passing through the wavefront is a straight line, i. e., the effective normal stress $P^* = P + Q = \alpha(V-V_0)$.

The gradient in the wavefront then adjusts itself so that $Q = a(V - V_0) - P$. If the curvature of the P, V relation is zero, the corresponding steady-state value of Q is zero; however, the rise time of the wave will depend upon the value of Q , as discussed in Section VI. In order to allow some freedom in adjusting the rise times to match experiment (Section VI-4), b has been given a small positive value. If rise times are of no interest, the value of b can be set equal to zero.

The curve BCD connecting the elastic curve AB with the solid curve GDE was chosen in the Murnaghan form (but with arbitrary K):

$$P = f_2(v) = P_1 + \frac{K}{R} \left[\left(\frac{V_1}{V} \right)^R - 1 \right] \quad (17)$$

Values of parameters used were $P_1 = 0.46$ kbar, $V_1 = 0.474$ cm³/g, $K = 12.06$ and $R = 2.0$ for 2.1 g/cm³ aluminum foam, and $P_1 = 0.23$ kbar, $V_1 = 0.576$ cm³/g, $K = 2.909$, and $R = 12.0$ for ATJ graphite foam. Equation (17) is a curve with positive curvature passing through P_1, V_1 which allows partial compaction between (P_1, V_1) and (P_2, V_2) and insures compaction to crystal density at (P_2, V_2) (see Section VI), where the resulting values of P and V are 4.5 kbar and 0.367 cm³/g for the aluminum foam, and 7.5 kbar and 0.433 cm³/g for the graphite foam. The values of P_1 and V_1 were determined experimentally (Section VI), while the values of the other constants were adjusted to be consistent with the attenuation experiments of Section VI-4 (rather than directly determined), and therefore are highly subject to the effects of any errors in the value of P_1 .

The equation used for curve GDE was of the form

$$P = f_3(v) = A \left(\frac{V_G}{V} - 1 \right) + B \left(\frac{V_G}{V} - 1 \right)^2 \quad (18)$$

where $A = 729$ kbar, $B = 1717$ kbar, and $V_G = 0.369$ cm³/g for the 2.1 g/cm³ aluminum foam, and $A = 193$ kbar, $B = 2855$ kbar, and

$V_G = 0.444 \text{ cm}^3/\text{g}$ for the ATJ graphite. The values of the constants for aluminum were inferred on the basis of extrapolation of the measurements of Al'tshuler et al.¹² and normalization of the data of Lundergan and Herrmann⁹ on 6061-T6 aluminum. In the case of ATJ graphite, the constants were chosen by normalizing the data of Doran.¹²

The compression process is assumed to correspond to a Hugoniot represented by the curve ABCDE specified by Eqs. (16) to (18). If expansion occurs before point B is reached in compression, it is assumed to occur along BA. If expansion occurs after point D is reached, it is assumed to occur along EDG.

For lack of better information it is assumed that if expansion occurs from any point C along BCD, it occurs along a path CF which is chosen according to the following prescription:

Along CF:

$$P = f_{\text{int}}(v) = P_c \left[1 + \frac{v - v_c}{v_c - v_{co}} + b \frac{(v - v_c)(v - v_{co})}{(v_c - v_{co})^2} \right] \quad (19)$$

where (v_c, P_c) is the point on BCD where compression stopped and expansion began, v_{co} is obtained from the simple proportion:

$$\frac{v_{co} - v_o}{v - v_o} = \frac{v_c - v_1}{v - v_1} \quad (20)$$

and the other quantities have the same values as specified previously. This recipe is simple and easy to compute and it forces the expansion curve to coincide with AB when C coincides with B. It effectively replaces Eq. (18) below point D, but the difference between the two curves is small between D and G. It is further assumed that if a reversal from expansion to compression occurs while the state point lies on FC, compression will proceed to point C and then along CDE as before.

NOREL Procedure for ATJ Graphite Target

In view of the results of the recovery experiments of Section VI, a modification of the calculation routine was investigated for ATJ graphite. The PHASETRANSITION procedure was not used because of the experimental observation that in contrast to the aluminum foams, graphite foams recovered to essentially their initial densities after being shocked in the pressure range of interest. Therefore, the NOREL procedure (see Appendix I) was to assume paths along ABDE (Fig. 4)

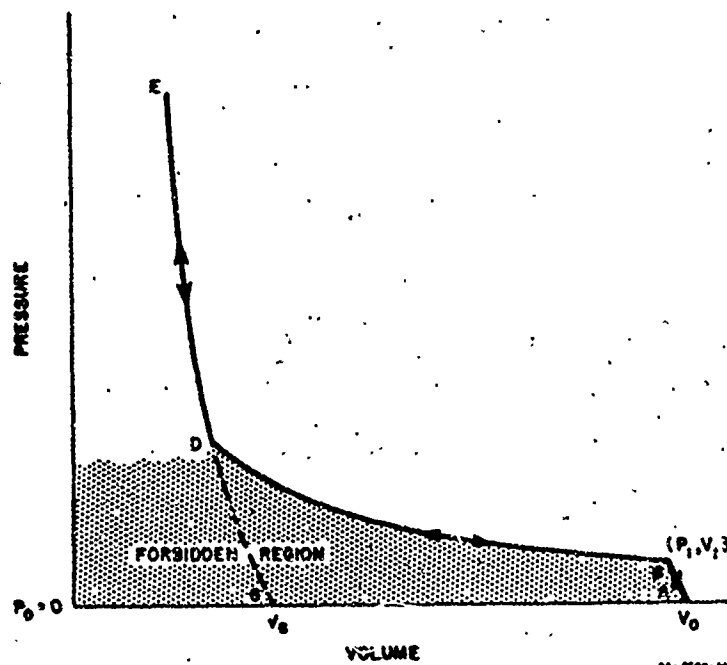


FIG. 4 ASSUMED P-V DIAGRAM IN NOREL PROCEDURE

for both compression and rarefaction waves. The equations used along AB, BD, and DE were the same as the compression curves discussed above, with the exception that along AB the value $b = 0.1$ was used for

compression but $h = 0$ was used for rarefaction, so as to avoid artificially introducing a rarefaction shock. (A flow chart is given in Fig. 25, Appendix I.)

SECTION IV

MATERIAL DEVELOPMENT

1. Specimen Fabrication

To perform reliable experiments, the target materials must have reproducible behavior and must be homogeneous on a scale small compared with their thickness. In the case of carbon and graphite materials we have of necessity relied upon the commercial supplier. ATJ graphite was chosen for most of the work because it provides the best combination of desired properties (i. e., homogeneity and yield strength). Other types of graphite and carbon were used for the parameter variation studies; although they were less desirable materials, X-ray transmission and volumetric density measurements indicated them to be reasonably homogeneous, with the exception of GA Coke carbon. All graphite or carbon foams were essentially of the "open cell" type (i. e., they were not impervious to the passage of gases).

In the case of porous aluminum specimens, a considerable amount of developmental work was done. Suitable aluminum foams are not commercially available. The only commercial aluminum foam used was MD-AK (see Appendix II), which was rather inhomogeneous, although its low density and high yield strength indicate it to be very promising as a shock pressure attenuator (see Section VI).

The major problem in making aluminum foams stems from the hard, nearly impervious oxide layer which forms on all aluminum surfaces. We have employed three techniques for producing homogeneous foams in the nominal density range of 40 to 80 percent of crystal density (depending on particle shape and pressure of pressing). These techniques are: (1) hot pressing of aluminum powders; (2) cold pressing of aluminum powders with subsequent sintering; and (3) repeated hot

pressing and sintering of a mixture of aluminum powders and thin-walled silica microballoons.

The hot pressing was accomplished by heating (to 450-570° F) aluminum powders of known particle size distribution in a hardened steel die and then pressing to the desired density (using 700 to 20,000 psi).

For technique 2, the aluminum powder was cold pressed (9500 to 13,000 psi) to essentially the desired final density. Thin specimens were pressed into solid aluminum rings (with 1/8-inch walls) for ease of handling. The sample disks were placed in a stainless steel box on graphite pads. The box was put in a furnace and an argon flow was maintained through the box. The temperature of the furnace was raised from room temperature to 1000° F over a period of five hours and held one hour at 1000° F; power to the furnace was then shut off. The furnace cooled to 200-300° F in about five hours, during which time the argon flow continued.

In the case of aluminum flake, the powder did not cold bond. It was therefore necessary to add a small amount of wax to make compacts that would hold together well enough to be handled. These compacts were heated more slowly to give the wax a chance to fume off. Maximum sintering temperature was 1000° F.

Under technique 3, aluminum powder and silica microballoons (walls about 2 microns thick) were mixed in an elbow blender and the mixture was placed in a graphite pressing die in a pot furnace. The temperature was raised to 900° F over a period of five hours. The die was then removed and the mixture was pressed at about 500 psi. The material was then returned to the furnace and heated to 1000° F, held one hour, removed and pressed to 500 psi, returned to the furnace at 1100° F for one hour, pressed again to 500 psi, and then allowed to

cool to room temperature. Densities achieved indicated that about half the porosity was due to the microballoons and half to ordinary gas-filled pores.

Except for the commercially obtained MD-AK all foams were essentially of the "open cell" type.

With Technique 2 it was easier and less expensive to control specimen quality than with Technique 1, although there is no inherent superiority of the method. Specimens were made in the shape of $3\frac{1}{2}$ -inch-diameter disks of various thicknesses and were subsequently machined to size if necessary (e. g., in the case of the quasi-static compression samples). Technique 3 was used only for foams of density ≤ 60 percent of crystal density.

2. Metallography and Quality Control

The metallographic method involved saw-cutting specimens (oriented parallel to and perpendicular to the pressing direction) from the sintered aluminum foam samples. Special care was taken to avoid deformation of the foam in the regions to be examined. The samples were vacuum-impregnated with epoxy resin and catalyst (Armstrong C-7). Surfaces were prepared by wet sanding on silicon carbide coated papers, 100 through 600 mesh, hand lapping with 30-micron alumina, and final polishing with 6-micron diamond. In some cases it was necessary to reimpregnate the polished surface with epoxy and repeat the sanding and polishing operations. The loose powder samples were mounted either in Lucite or in epoxy, depending on the nature of the particles. The particle sizes observed in the foam samples correspond to the screen fraction used and to the particle size and shape observed in the powder mounts; hence it is reasonable to assume that the structure of the foam observed is real and not the result of gross distortion, cold flow, etc.

Types of powders used and the resulting foams are shown in the photomicrographs of Figs. 5 and 6. No differences were noticed between photomicrographs taken at orientations parallel to and perpendicular to the direction of pressing. The small dark spots in the particles of Figs. 6a and 6c are probably polishing pits.

In addition to the metallographic examination, selected specimens were checked for uniformity of density by either X-ray transmission or sectioning and weighing. Longitudinal acoustic velocities were measured (see Sections V and VI) for each specimen as a means of quality control.

The aluminum powder used in the foam for which the detailed Hugoniot measurements to 25 kbar were made (see Fig. 6a, b, c) and on which the attenuation studies were performed was the "chunk" powder type MD801 (see Appendix II) of crystal density 2.71 g/cm^3 . The manufacturer's spectroscopic analysis disclosed the composition to be:

Al	99.5%
Fe	0.15
Si	0.06
Zn	0.02
O	0.27

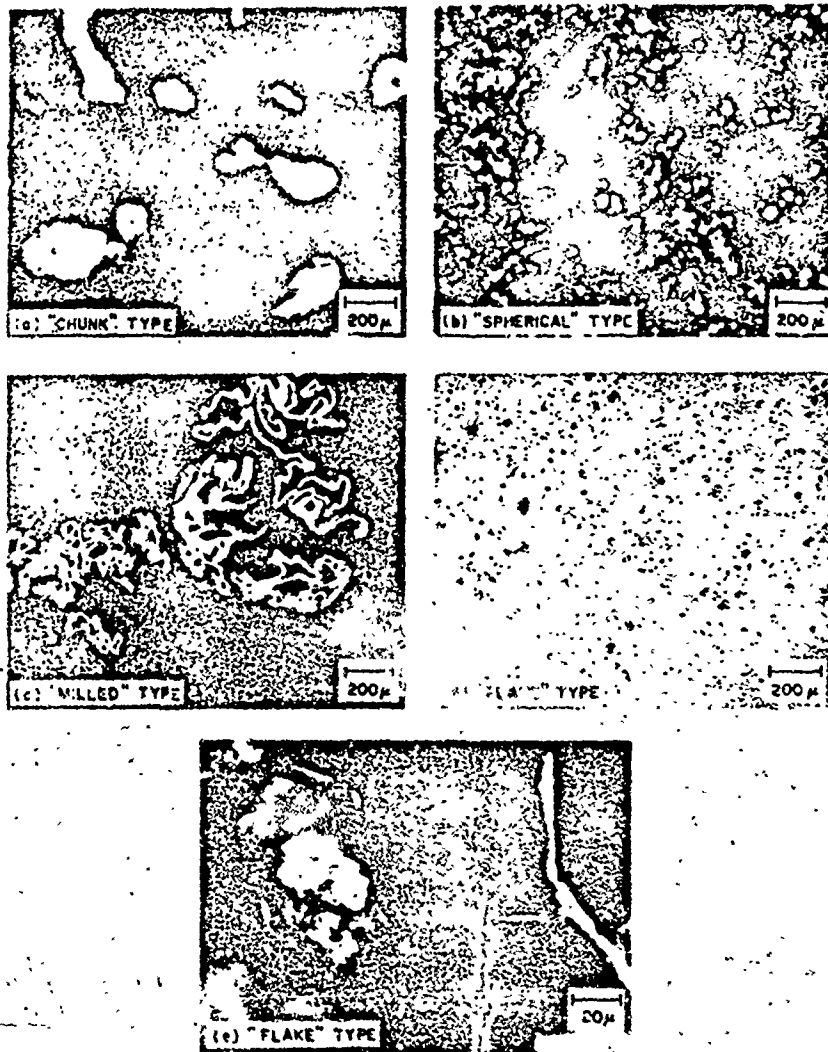


FIG. 5 POWDERS USED FOR MAKING SINTERED ALUMINUM FOAM

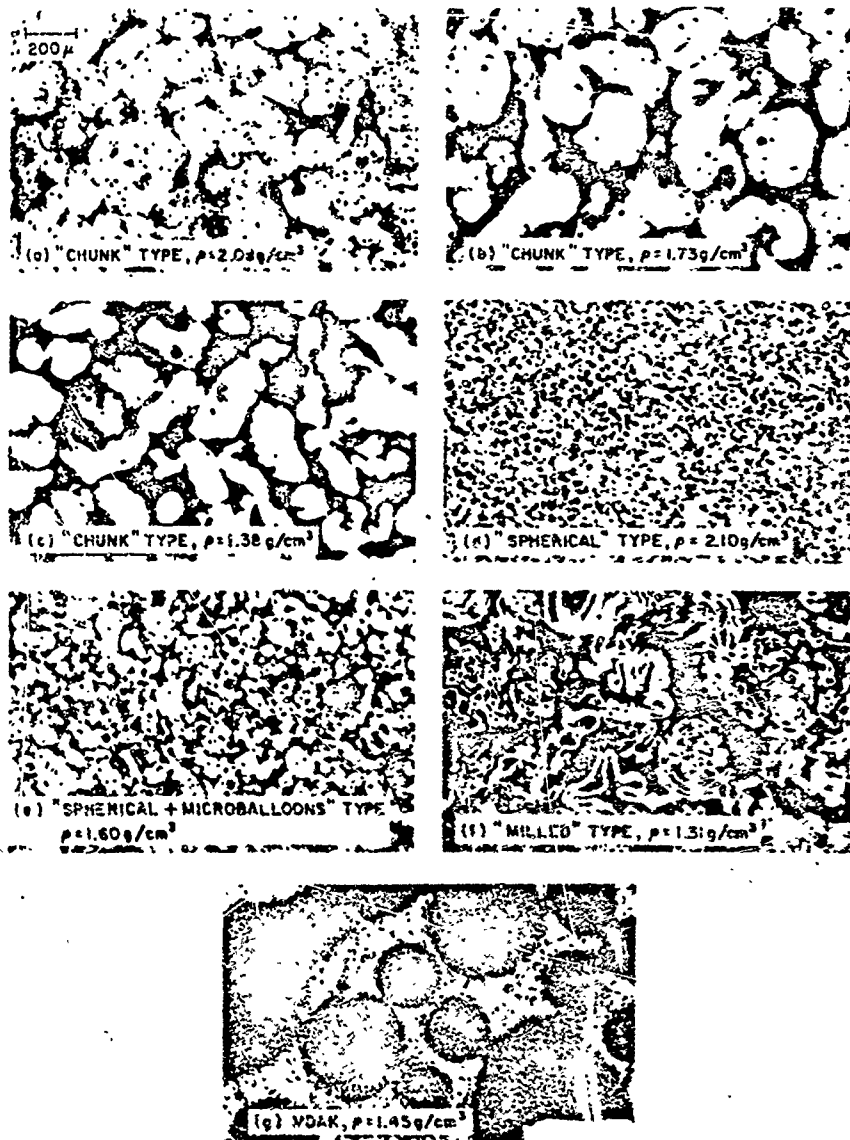


FIG. 6 TYPICAL ALUMINUM FOAM TYPES

SECTION V

EXPERIMENTAL TECHNIQUES

1. Shock Wave Measurements

a. Technique for Measurement of Hugoniot Points

All Hugoniot measurements (including the parameter variation studies) employed the impedance-match method (see Fig. 7). The projectile (made from 2024-T351 aluminum, a material with a reasonably well known Hugoniot*) was accelerated to a velocity u_A and impacted

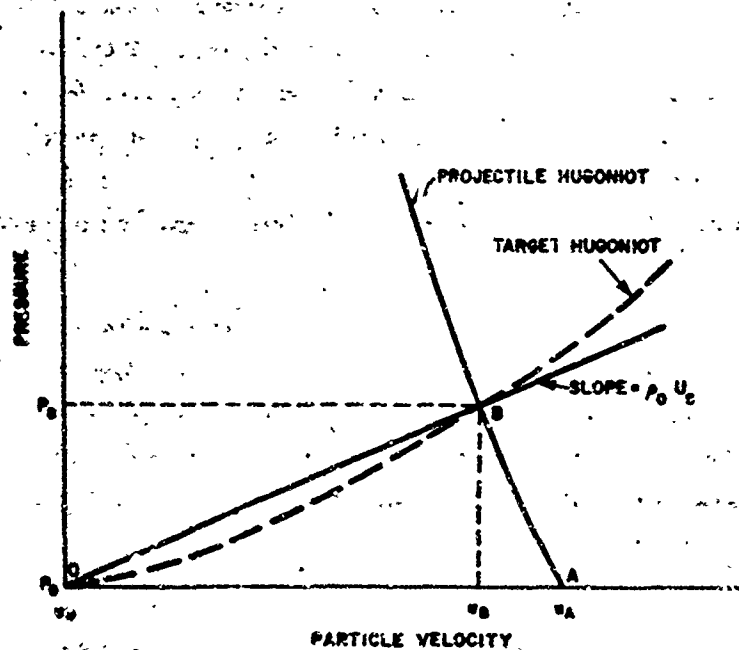


FIG. 7 ILLUSTRATION OF IMPEDANCE-MATCH METHOD FOR MEASURING TARGET HUGONIOT

* Extrapolation of the data of Fowler^{1,2} for 2024-T4 aluminum, in conjunction with other data at 5, 13, and 17 kbar.

the target material. The initial state in the projectile is represented by point A of Fig. 7, and the initial state in the target material is represented by point O. The conservation relations (jump conditions) require that upon impact both materials must reach the pressure-particle velocity state represented by point B. Conservation of momentum requires that across a single shock

$$\frac{P_B - P_0}{u_B - u_0} = \rho_0 U_s$$

where ρ_0 is the initial density of the target material and U_s is the velocity of a shock of amplitude characterized by P_B and u_B in the material. Thus, measuring the shock velocity experimentally and knowing the initial density of the target, a line through point O can be drawn with slope $\rho_0 U_s$. At point B this line intersects the known projectile Hugoniot drawn from point A. Therefore, point B must lie on the Hugoniot of the target. Using different projectile velocities (i. e., various values of u_A), we can trace out the entire Hugoniot for the target material.

If P_B of Fig. 7 is less than P_c of Fig. 1, a single shock is unstable and the pressure pulse in the target will consist of two fronts, one of amplitude P_E (P_c of Fig. 1), and the other of amplitude P_B . The determination of the target Hugoniot is then more complicated, but if $P_E \ll P_B$ no great error will be introduced by adopting the following procedure, as illustrated in Fig. 8.

1. Measure P_Q with a quartz gage, as described below.
2. Measure Γ or U_s and draw a line through O with slope $\rho_0 (U_s)$ (point E is as yet undetermined).
3. On the basis of other cross-curve data, obtained at higher pressures, estimate the cross curve from the line found in step 2 to point Q measured in step 1. This fixes point E.

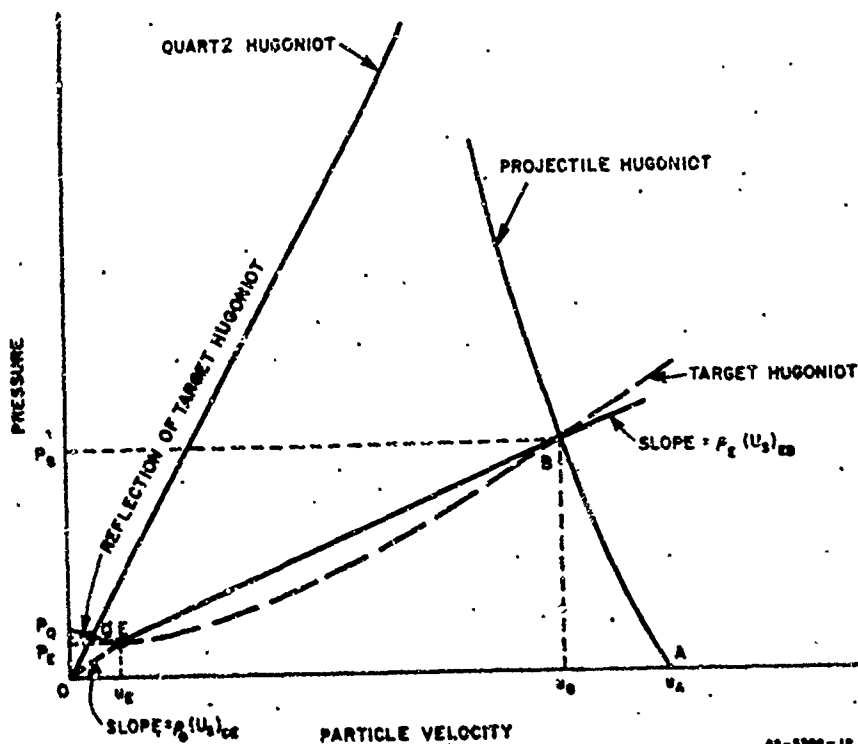


FIG. 8 ILLUSTRATION OF PROCEDURE FOR HUGONIOT MEASUREMENT WHEN A DOUBLE WAVE STRUCTURE EXISTS.

4. Calculate ρ_E from the jump conditions and draw line EB.
5. Proceed as in single shock case.

If $P_B = P_E$ the uncertainty in the estimated cross curve becomes very important; iteration may help. A serious problem is also introduced because $(U_s)_{EB}$ will be in error due to reverberations of the forerunner between the quartz gage and the main wavefront. If $P_B \gg P_E$, however, the uncertainty in the cross curve is of rather minor importance, and not only will the reverberations of the forerunner

occur over a relatively small percentage of the total transit time over which $(U_s)_{EB}$ is measured, but each reverberation results in only a small perturbation in $(U_s)_{EB}$.

Implicit in this entire development is the assumption that steady state has been reached. Furthermore, since shock velocities are measured as averages over the transit time in the specimen (see below) considerable error may be introduced if steady state has not been achieved in a time short compared with the total transit time. The situation is clarified, however, by repeating experiments with different target thicknesses but the same projectile velocity. In the experiments reported herein, forerunner pressures (P_0) have not been found to be as reproducible as desired; however, confirmation of Hugoniot points for $P_2 \gg P_0$ has been excellent (see Section VI).

Except where noted, all experiments employed quartz gages as the primary sensing element. The quartz gage is an electroded (with guard ring) X-cut synthetic quartz disk. Current from X-cut quartz crystals may be used as a sensitive indicator of stress-time profiles, as discussed in detail by Graham et al.¹³ The current amplitude and its time dependence are functions of the dielectric, piezoelectric, and mechanical properties of shock-loaded quartz.

The normal stress difference between the two faces of the disk is given initially by the relation

$$\Delta P = \frac{V^2}{RAKU} \quad (21)$$

where V is the potential drop across the total load resistance R through which the piezoelectric current flows; l is the thickness of the disk; A is the active electrode area, K is an experimentally determined current coefficient, and U_s is the shock velocity in quartz. Values of

U_g and K are given by Graham et al.¹¹ as a function of stress.* Rather than using their suggested average values for each pressure range, we have chosen to draw best-fit curves to their data; the discrepancy is small, however. For the quartz gages used in our experiments, $A = 0.201 \text{ in.}^2$, $l = 0.376 \text{ in.}$, and $R = 51.0 \Omega$, so that Fig. 9 may be used to determine the normal pressure at the specimen-quartz interface from measurement of the voltage across R .

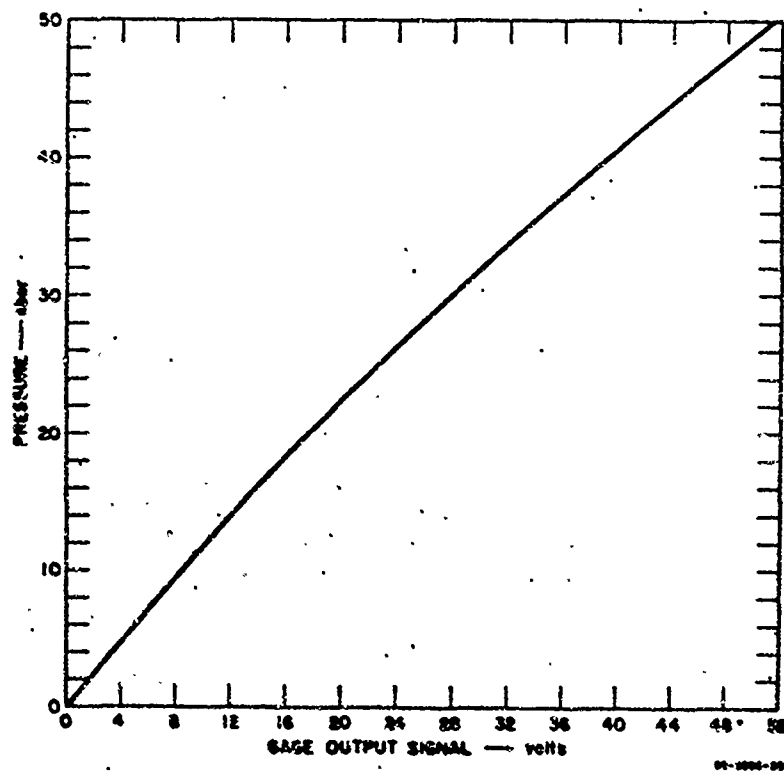


FIG. 9 CALIBRATION CURVE FOR QUARTZ GAGE WITH: $A = 0.201 \text{ in.}^2$, $l = 0.376 \text{ in.}$, AND $R = 51.0 \Omega$

as a function of time. As the shock propagates through the quartz, the curve of Fig. 9 will shift continuously in the direction of higher voltages

* The values of K above 18 kbar and of U_g above 25 kbar show some scatter, however, so that computed pressures are probably less reliable at the higher pressures.

for the same pressure, perhaps reaching as much as a 7-percent increase for transit of a 20-kbar shock, so that pressure-time profiles may be distorted and corrections should be made to avoid errors in interpretation. Since the magnitude of the shift depends on shock amplitude within the quartz disk, results for the second wave of a double wave profile should not be affected much by the passage of low-amplitude forerunner waves. As described below, the gage was surrounded with potting material which approximates the shock impedance of quartz, so that for the shock attenuation experiments the useful lifetime of the gage could be extended by reconstructing approximate profiles (i. e., since the voltage is proportional to ΔP , the value of P at the specimen-quartz interface could be estimated by adding the stress value found one transit time earlier--that is, 1.66 μ sec earlier).

Average shock velocities were determined from the time interval between tilt pin closure (see below) and the time at which the profile for each shock reached half its total associated pressure increment (see diagram accompanying Table VI, Appendix III). The use of this "half-wave point" for measuring velocity can be argued on the basis of the profile shapes (see Fig. 21) and has the fortunate advantage of providing the least opportunity for random reading errors.

b. Experimental Details

Target Preparation. The prime constituents of the target assembly are the specimen, the adapter ring, the tilt pins, the sensing element (quartz gage), and the radial velocity pins (see Figs. 10 and 11). Each specimen was lapped to a tolerance of 0.02 mm to 0.0002 mm (depending on specimen material and projectile velocity) and then attached to a prefabricated molded support, which was thick enough to prevent bowing of the specimen (see Fig. 10). This support was constructed from a mixture of Armstrong C-7 epoxy and glass beads

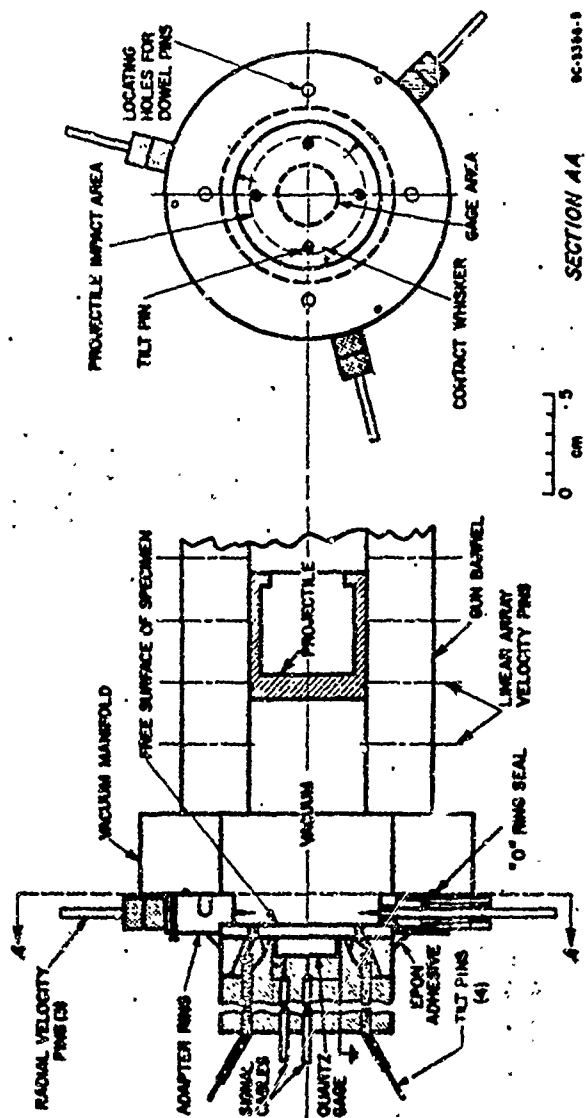


FIG. 19. TARGET CONFIGURATION IMMEDIATELY PRIOR TO IMPACT

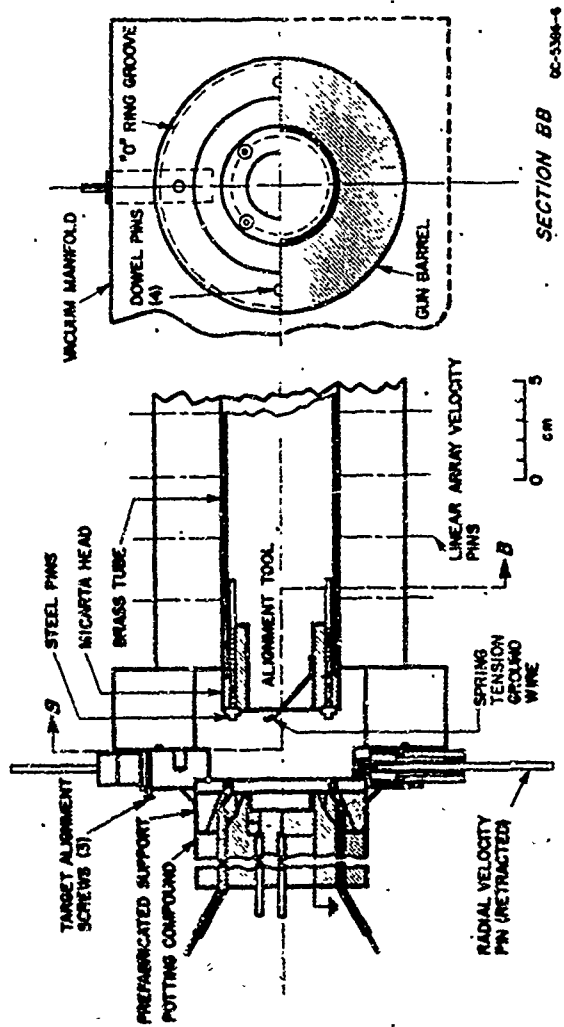


FIG. 11 CONFIGURATION OF GAS GUN PRIOR TO TARGET ALIGNMENT

(40 μ to 75 μ size range) in a proportion adjusted to approximate the shock impedance of the quartz gage. A thin layer of quick-setting epoxy was applied to the lapped surfaces of the molded support and the specimen, which were held in contact by a uniform pressure until the cure cycle for the adhesive was complete.

The four tilt pin clearance holes were drilled at 90° intervals using a guided No. 51 drill; the tilt pin wires (copper, No. 22) were bent and inserted through the rear face of the specimen until they extended about 1 mm beyond the impact surface. The bared portion of each tilt pin was supported near the center of the clearance hole by the insulation (which covered the conductor for approximately half its length in the specimen). Quick-setting epoxy was used to fill to excess the remaining volume between the pins and the walls of the clearance holes, so as to give good bonding for positive location and mechanical support. On the rear surface of the specimen the conductors were also potted with quick-setting epoxy for support.

After the pins had been permanently located with respect to the specimen, the excess potting material and pin lengths were removed by filing and lapping until the leading surface of each pin lay within 0.002 mm of the plane defined by the impact surface of the specimen as determined by a dial gage. Any small deviation from this plane was noted and considered when the shot data were reduced.

The quartz gage was clamped firmly in place on the rear surface of the specimen, and a small amount of viscous quick-setting epoxy was applied around its circumference. The resulting bond held the gage in place during subsequent potting and formed a seal that did not allow any potting material to seep between the gage and the specimen. To check that the gage was in good contact with the specimen, a combined thickness measurement was made across the specimen and gage and was compared with the sum of their individual thicknesses.

After the attachment of an electrical ground and the necessary signal cables and bias resistor, the assembly was potted with the previously described epoxy-glass bead mixture. When the potting compound had cured, electrical checks were made to determine if there were any shorted pins or faulty connections. The assembly was placed in a carefully machined recess in the adapter ring and fixed in place with Shell Epox (No. 911F) adhesive, which provided a vacuum-tight seal.

The adapter ring was also used to locate the three retractable radial velocity pins. These pins were located by using high-precision guide holes in the adapter ring to define a plane parallel to that of the specimen at an accurately measured distance of about 6 mm. The discharge of these pins upon contact with the projectile was detected and recorded as described in detail below.

Projectiles. The 7.6-cm-long, hollow 2024-T351 aluminum projectiles used in all Hugoniot shots (see Fig. 10) were fabricated on a lathe and subsequently placed in a close-fitting guide ring for machine lapping. Final squareness and flatness of the projectile head were generally held to within 0.002 mm. Projectile heads were either 6 mm or 12 mm thick. For the shock attenuation shots it was desired to impact the target with a short-duration, high-amplitude pressure pulse rather than the flat, long-duration pulse provided by thick projectile heads. To this end, 0.0160-inch-thick 6061-T6 aluminum flyer plates were prepared in the form of 2.36-inch-diameter disks. Each flyer plate was mounted on a 1-inch-thick piece of low density (2 lb/cu ft) styrofoam, which in turn was mounted on the head of a modified 2024 aluminum projectile (see Fig. 12). Care was taken to mount the flyer plate perpendicular to the projectile walls.

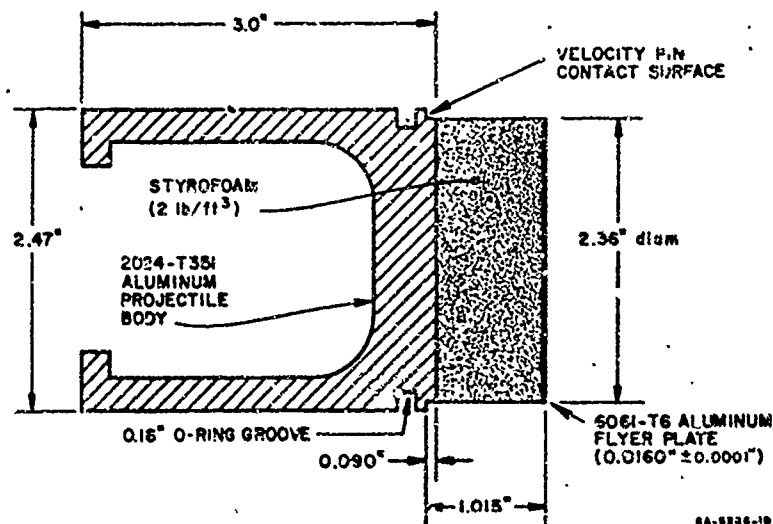


FIG. 12 PROJECTILE ASSEMBLY FOR SHOCK ATTENUATION STUDIES

By use of this flyer plate assembly, it was possible to achieve relatively plane impacts with the desired pulse length ($\sim 0.15 \mu\text{sec}$) and input momentum densities ($\sim 0.5 - 0.75 \times 10^4 \text{ dyne-sec/cm}^2$). The styrofoam support could produce only a very minor perturbation on the shock profile,* and the 2024 aluminum projectile could play no role whatever during the times at which profile measurements were made. All profile measurements employed the quartz gage techniques described below.

Target Alignment Procedure. It is extremely important to minimize the relative tilt between projectile and target because shock wave velocities are typically an order of magnitude greater than the associated particle velocities even for foams at the shock strengths used in this study.

* The effect of the styrofoam was implicitly taken into account in the attenuation calculations (see Section III); a comparison of calculated shock profiles with and without the styrofoam support is given in Section VI.

The target assembly was mounted on the muzzle end of the gun, the position of the target being controlled by four close-fitting dowel pins, and three fine-threaded alignment screws. A reference plane perpendicular to the axis of the gun barrel was provided by the alignment tool (see Fig. 11). The screws were used to rotate the free surface of the specimen into this plane without breaking the vacuum seal.

The alignment tool is a 46-cm brass cylinder that closely fits the bore of the gun barrel. The precise clearance required is controlled by using three adhesive cellophane tape strips spaced 120° apart on the circumference and extending the length of the cylinder. A short cellophane flap extends onto the ends of the tool. The build-up of these strips involves the use of two or three layers of tape, each in turn being cut to length from material 5 mm wider than the previous layer.

Four adjustable hardened steel pins and a light spring tension ground wire are mounted on a Micarta head attached with an epoxy adhesive to one end of the alignment tool. The steel pins are adjusted and hand-lapped to within 0.002 mm of each other. Electrical conductors extend from the pins out through the breach plug of the gun to a 12-volt power supply and four indicator lamps. Contact of each pin with the (conductive) specimen completes a circuit that turns on a specific indicator lamp. Contact pressure is supplied by a weak spring located between the breach plug and a long rod "handle" behind the brass cylinder.

The target alignment procedure (see Fig. 11) consisted of (1) sliding the alignment tool down the gun barrel until it contacted the target, (2) evacuating the system, (3) turning the three fine-threaded alignment screws until contact between the adapter ring and the vacuum manifold was broken (the ends of the screws and the "O"-ring then provided total support for the target assembly), and (4) adjusting the alignment screws until all four indicator lamps were glowing uniformly.

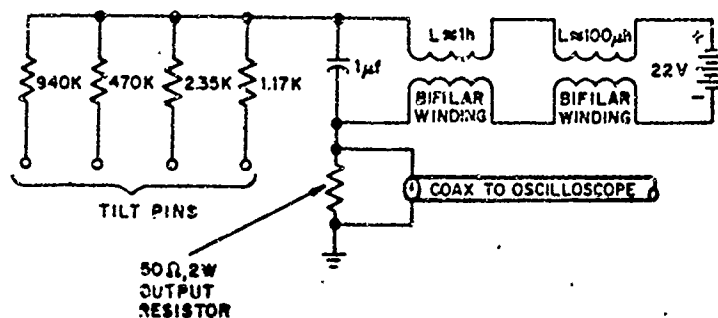
The alignment was checked by venting the gun barrel to atmospheric pressure and rotating the alignment tool by 120° , 240° , and 360° (re-evacuating each time).

If all four lamps were lit for all three positions of the alignment tool, the target was perpendicular to the axis of the gun barrel to within about 0.002 mm. The failure of all four lamps to light simultaneously after rotation of the alignment tool was an indication that the target was not flat to the required tolerances. The deviation from flatness could be estimated by the amount that the alignment screws must be turned in order to light the unlit lamps in the rotated configuration.

The tilt pin arrangement described above allowed the measurement of both magnitude and orientation of tilt. Each pin was charged to + 22v, and discharged upon contact with the (conductive) projectile. To display the occurrence times of electrical pin closures unambiguously, a binary coded system was employed (see Fig. 13). The tilt pins were charged by a $1\mu\text{F}$ capacitor that formed part of an RLC circuit. When each pin was grounded it discharged through a different resistor, resulting in a different current and ultimately a different measured voltage across the $50\ \Omega$ output resistor. * The signals from the four pins were conveyed through a single cable and displayed on an internally triggered, cathode-modulated (see below), fast-rise oscilloscope sweeping at $0.1\ \mu\text{sec/cm}$ (see Fig. 14a). As the flatness of impact is improved, the voltage steps become more and more coincident until only one large step is seen (Fig. 14b).

Projectile Velocity Measurement. The first Hugoniot shots fired (Shots 11, 117 to 11, 316) employed a linear array of electrically charged

* The resulting signals are given relative amplitudes of 1, 2, 4, and 8 (see record of Fig. 14a) by use of the circuit resistors specified in Fig. 13.



GA-5000-21

FIG. 13 BINARY CODER CIRCUIT FOR DISTINGUISHING ELECTRICAL PIN CLOSURES

contact pins which extended through the side of the gun barrel and were discharged through the projectile (see Fig. 10) for deducing projectile velocities. The measured times at which these pins discharge were used to compute projectile velocity and acceleration; the results were then extrapolated to determine the velocity at time of impact. Subsequent Hugoniot shots employed the more accurate radial velocity pin system pictured in Fig. 10. The radial velocity pins are retractable brass rods with 0.25-mm-diameter "whisker" ends that are electrically charged to + 100v and operate through a circuit similar to that of Fig. 13. They lie in a plane 6 mm from the impact surface of the target and may be extended radially into the path of the projectile after the target has been aligned (see Figs. 10 and 11). The final position of each pin is controlled by a carefully machined shoulder in each guide hole (see Fig. 10). Timing signals are produced when the charged pins are grounded upon physical contact with the conductive projectile (which, in turn, is coupled to ground through the gun barrel). One of the radial pins is 0.05 mm farther from the target and connected to ground.

The radial pin signals were displayed on an internally triggered, cathode-modulated, fast-rise oscilloscope sweeping at 0.1 μsec/cm.

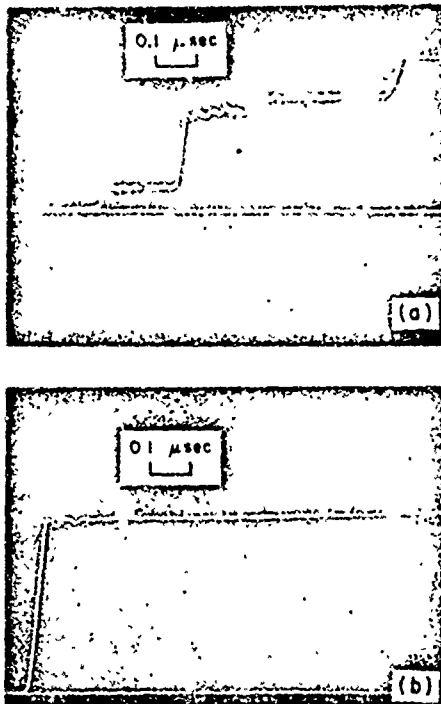


FIG. 14 OSCILLOSCOPE RECORDS SHOWING TILT PIN CLOSURES AND CATHODE MODULATION TIME MARKS
 (a) Target not precisely aligned; order of pin closure is 2, 8, 1, 4.
 (b) Target aligned; pin closures are essentially simultaneous.

This allowed small positioning errors in the pins to be averaged out and also allowed tilt of the projectile to be taken into account in the velocity computations.

The first radial pin closure signal also started a 10-mc counter and was displayed on a raster oscilloscope. The first tilt pin closure stopped the counter and was displayed on the raster oscilloscope. The information thus obtained, when used in conjunction with the cathode-modulated, binary-coded oscilloscope records, was sufficient to

calculate to within about $0.01 \mu\text{sec}$ the time interval between the projectile arrival at the plane of the radial pins and the impact with the target (see below).

Time Correlations. It is important to establish a well defined time base, so that correlations can be made between events recorded by different instruments. If an oscilloscope trace has a fiducial mark occurring every $0.50 \mu\text{sec}$, then two separate events, such as the closing of a tilt pin and the occurrence of a quartz gage signal, may be individually recorded on different oscilloscopes set to trigger internally or through some delay. These oscilloscopes may be set to sweep at $0.1 \mu\text{sec/cm}$ so that much detail is resolved. If the relative occurrence times of events are known to the nearest half-microsecond (perhaps from a slow-sweeping oscilloscope), the fiducial marks may be used to provide the necessary accurate correlation, provided the fiducial marks themselves are accurately controlled.

The cathode modulation timing system described below minimizes errors due to variations in oscilloscope sweep speeds and trace linearity, and is capable of providing time correlations between oscilloscopes to within $0.01 \mu\text{sec}$. Care must be taken, however, to employ the normal precautions to prevent high-frequency noise from appearing in the data signal traces (i. e., use shielded cables, ground oscilloscope chassis etc.).

The time marks originate from an E-H Model 120D pulse generator* capable of supplying pulses $0.01\text{-}\mu\text{sec}$ wide. The pulse generator was controlled by an external high-stability, temperature-compensated, 2-mc crystal oscillator. The timing pulses were used to modulate the cathode bias voltage of the oscilloscope CRT's (see Fig. 15). Pulse

* Manufactured by E-H Research Laboratories, Inc., Oakland, California.

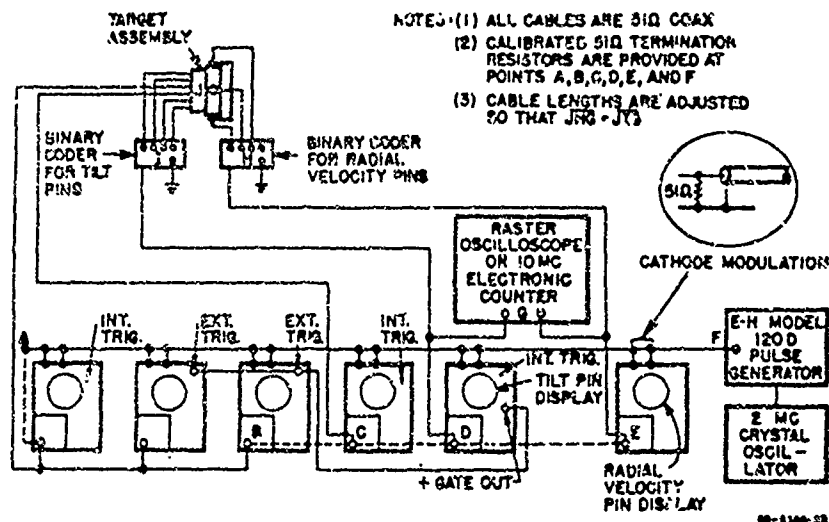


FIG. 15 BLOCK DIAGRAM OF INSTRUMENTATION FOR RECORDING AND CALIBRATING DATA SIGNALS

amplitudes were adjusted so that the time marks were represented by blanking of the oscilloscope traces at 0.5- μ sec intervals. To allow correlation of different signals, the electrical cables labeled in Fig. 15 were chosen to be of the same type and have lengths such that

$$\overline{JB} = \overline{JC} = \overline{BC} = \overline{JD} = \overline{BCD} = \overline{JKE} = \overline{BCDE}, \quad (22)$$

The lengths of the other cables shown in Fig. 15 were not important, since the calibration procedure compensates for their effects.

The calibration procedure involved connecting all the dotted cables as indicated in Fig. 15 and removing the termination resistors at A, B, C, and D, while leaving the oscilloscope sweep speed settings and all other cables and delay units the same as during the gun shot. Oscilloscope records made with the system in this configuration appear as in Fig. 16a, where a cathode modulation timing mark occurs at time t_0 on the trace, and the maximum of the blanking pulse which produced the time mark is displayed at time t_1 . The interval $(t_1 - t_0)$ represents the sum of the internal delays in the oscilloscope and the time delays associated with external delay units and the

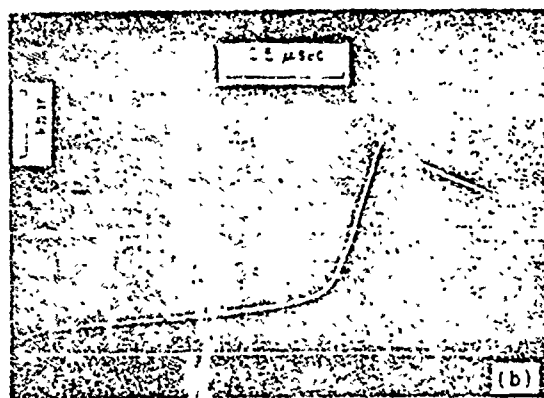
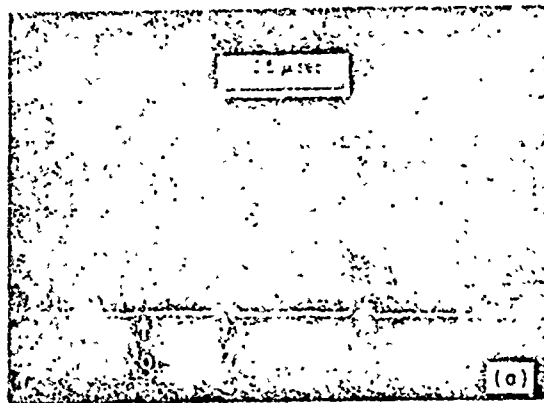


FIG. 16 (a) CALIBRATION RECORD FOR CATHODE MODULATION
TIMING SYSTEM
(b) QUARTZ LUGE RECORD WITH CATHODE MODULATION
TIME MARKS (Scale: 11,65)

extra length of cable through which the pulse must travel between the cathode and the vertical input terminal of the oscilloscope. A comparison of the value of $(t_1 - t_0)$ for each oscilloscope was used to adjust the shot data to a common time base.* Since the time marks were used at 0.5- μ sec intervals only, a 10-mc sine wave was used to check linearity of the oscilloscope sweep between time marks. A typical oscilloscope record from a quartz gage shot using cathode modulation time marks is shown in Fig. 16b. Shots 11,269 to 11,799 employed the time mark system described above.

2. Measurement of Longitudinal Sound Velocities

Figure 17 shows a block diagram of the sound velocity measuring system. A 0.6- μ sec square-wave pulse from a pulse generator is converted into small-amplitude approximately sinusoidal mechanical waves of 1 mc/sec frequency by a set of two independent piezoelectric (PZT-4) crystals contained in the mercury delay line and the sample holder. The mechanical waves traverse their respective media and are reconverted into electrical signals by the second set of PZT crystals. These "output" signals may be viewed on an oscilloscope; their difference is found by the Type 1A1 amplifier. The length of the Hg column is carefully adjusted so that this difference equals zero (i. e., Signal A = Signal B); the system is then nulled and the time delay through the mercury and the sample are the same.

The longitudinal velocity of sound in mercury (1.446 mm/ μ sec at 25°C) is accurately known and quite insensitive (-0.000465 mm/ μ sec/°C) to reasonable temperature changes; thus it makes an ideal medium for comparison purposes. The "null method" for determining the velocity of sound in a solid material requires that:

* If the cable lengths satisfy Eq. (22), a common time base is established by simply subtracting the appropriate value of $(t_1 - t_0)$ from the times indicated by the cathode modulation time marks in each shot record.

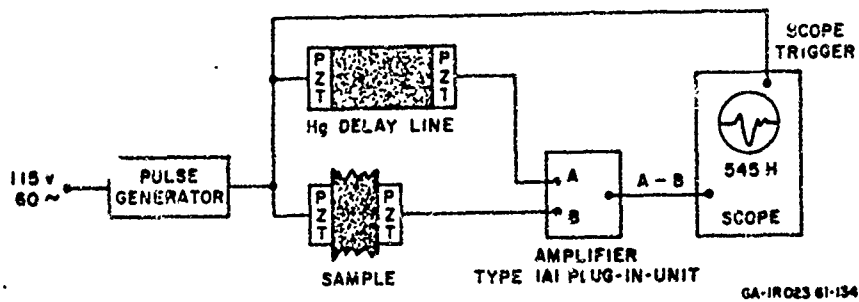


FIG. 17 BLOCK DIAGRAM OF SYSTEM FOR MEASUREMENT OF LONGITUDINAL SOUND VELOCITY

$$t_{Hg} = t_c$$

where

t_{Hg} = delay time through the mercury

t_s = delay time through the sample

thus,

$$\frac{d_{Hg}}{v_{Hg}} + t_{oHg} = \frac{d_s}{v_s} + t_{os}$$

where

d_{Hg} = path length through the mercury

v_{Hg} = 1.446 mm/ μ sec at 25°C.

t_{oHg} = time delay at zero thickness of the mercury column (constant)

d_s = path length through the specimen

t_{os} = time delay at zero thickness of the specimen holder (constant)

v_s = the longitudinal (sound) velocity being measured,

which is written as

$$v_s = \frac{d_s}{\frac{d_{Hg}}{v_{Hg}} + t_{oHg} - t_{os}} \quad (23)$$

and the sound velocity (v_s) reduces to a function of path lengths, i. e., d_s and d_{Hg} . The value d_s is determined independently of the electronic measurements by direct measurement of the specimen's dimensions. Several different thicknesses of specimens were used to eliminate any uncertainties associated with transducer-specimen coupling.

AFWL-TR-66-13

- This page intentionally left blank.

SECTION VI

EXPERIMENTAL RESULTS AND DISCUSSION

1. Parameter Variation

The parameter variations are illustrated in part by the photomicrographs shown in Section IV. A wide range of densities and particle (or pore) shapes, sizes, and size distributions was investigated. Unfortunately, there is too much scatter in the data (see Appendix III) to allow specific conclusions as to the effect of any single parameter alone in the above list; however, certain general observations can be made.

a. MD-AK aluminum, which has the strongest matrix (solidified molten aluminum, rather than the weaker sintered bonds between particles--see Figs. 6 and 7) has the largest precursor amplitude and speed, despite its low density (1.45 g/cm^3). The situation is not entirely clearcut because MD-AK has large spherical-type pores rather than small irregular ones as do the sintered materials. However, our preliminary results indicate the pore shape, size, and size distribution to be of less importance than matrix strength.

b. For both graphite and sintered aluminum foams, the precursor amplitude and speed decrease with increasing distention, but experiments on aluminum foams show that distention alone may not be as important as matrix strength, which may be expected to depend upon the manufacturing process.

c. In the pressure and porosity range studied for each type of foam, dynamic data show that the "compacted" volumes for pressures above a few kilobars are essentially those of the solid materials, regardless of particle (or pore) shape, size, or size distribution,

resulting in the plots of Figs. 18 to 20 (see Section VI-C). Possible exceptions are MD-AK (for which we do not have reliable Hugoniot points), aluminum flake (one shot only; see also Footnote a to Table III), and GA Coke carbon (one shot only; see also Footnote c to Table III). Points representing compacted ATJ graphite show no dependence on orientation and have not been labeled with orientation in the figures. (Orientations are given in Appendix III.)

d. Dynamic elastic limits scale approximately with quasi-static elastic limits and lie generally within a factor of three of the quasi-static values. Some scatter is present in the data, however.

e. Precursor velocities are generally higher in foams which have higher elastic limits. Quasi-static yield stress may prove to be a reasonable indicator of relative precursor velocities for a given type of material.

f. Measured longitudinal acoustic velocities (see Section V-B) tend to be qualitative indicators of elastic wave velocities, but are generally larger than the elastic wave velocity, as might be expected for foams (see Tables V to VII in Appendix III).

It should be noted that Lockyer¹⁸ has investigated nondestructive methods for evaluation of graphite materials (including ATJ graphite) and found correlations between such quantities as longitudinal sound velocity, bulk density, electrical resistivity, tensile elastic modulus, ultimate tensile strength, and dynamic elastic modulus in flexure. Thus, it is reasonable to suppose that some inexpensive, nondestructive tests may prove useful indicators of shock forerunner amplitudes and speeds.

3. Terminal Observations on Recovered Material

All of the shots fired were designed for the purpose of making dynamic measurements on the foams. However, in many cases pieces

of the targets which had experienced both the initial shock and the shock reflected from the foam-quartz interface were recovered in a condition suitable for measurements of density.

Results are shown in Table I, where the column headed " P_{max} " contains the range of maximum pressures of reflected shocks experienced by material for which the reported recovered densities were actually measured. In the case of "chunk" aluminum and ATJ graphite, the values reported for recovered density are based on the average for several recovered targets. In the case of all other materials the value reported is based upon data for only one or two shots. Table II contains recovered density information for quasi-statically compressed (with sides confined) specimens to serve as a basis for comparison. These data should be considered as only approximate typical values. In many cases the data are based on only one experiment.

The results are very striking. Sintered aluminum foams evidently "lock" at close to solid density, whereas graphite foams (particularly ATJ) recover their porous character. Both kinds of foam are of the open cell type (as determined by a vacuum integrity test), so that the behavior of graphite as contrasted with that of aluminum is rather interesting. The MD-AK aluminum, on the other hand, is a "closed cell" type of foam, so it would be expected that gases would be trapped in the pores during shock compression. It is not known, however, whether the lower density of the recovered MD-AK material is due to "spring-back" or whether the foam was never fully compacted.

These results for graphite and sintered aluminum foams have been used in estimating release curves for the shock attenuation calculations (Section III); results are given in Section VI-D. The "spring-back" phenomenon in graphite might be of further interest because it offers the possibility of a countermeasure material which can function for more than one "hit."

Table I
DENSITY DATA FOR RECOVERED SHOCKED FOAMS

Material	Estimated* P_{max} (kbar)	Initial Density (g/cm ³)	Typical Recovered Density (g/cm ³)	Density of Solid Material (g/cm ³)
<u>Aluminum:</u>				
Chunk (148-420 μ)	15, ..., 60	2.09	2.65	2.71
Milled (250-840 μ)	5-10	1.08	2.6	2.7
Spherical (5-106 μ)	5-10	1.74	2.6	2.7
Spherical (44-106 μ) + Microballoons (44-106 μ)	5-10	1.63	2.6	2.7
WD-AK	5-10	1.45	2.3	2.7
MD-AK	30-70	1.45	2.3	2.7
<u>Graphite:</u>				
ATJ	10, ..., 50	1.73	1.7	2.2
Grade 60	~ 25	1.02	1.85	2.2

* Estimated at quartz-foam interface as described in Section VI-3.

Table II
RESIDUAL DENSITIES OF QUASI-STATICALLY COMPRESSED FOAMS

Material	P_{max} (kbar)	Initial Density (g/cm ³)	Typical Density at P_{max} (g/cm ³)	Typical Recovered Density in Die (g/cm ³)
<u>Aluminum:</u>				
Chunk (149-420 μ)	1.8	2.09	2.5	2.5
Milled (250-840 μ)	1.8	1.03, 1.40	2.5	2.45
Spherical (5-106 μ)	1.8	2.11	2.56	2.56
Spherical (44-106 μ) + Microballoons (44-106 μ)	1.8	1.29	2.38	2.33
MD-AK	4.3	1.45	2.42	2.31
<u>Graphite:</u>				
ATJ	1.8	1.72	2.12	1.73
Grade 60	1.0	1.02	1.94	1.59

3. Hugoniot of Foams*

The plots of Figs. 18 to 20 are comprised of points representing macroscopic pressure-particle velocity states for various graphite and sintered aluminum foams. In all cases the Hugoniot points were determined by the impedance-match method as discussed in Section V, and only the most reliable points available have been plotted. Typical voltage-time profiles measured with quartz are shown in Fig. 21. Foam targets of substantially different thicknesses yielded the same Hugoniot (i. e., yielded essentially the same shock velocity for the same impact conditions), indicating that the shock velocities used for determining the Hugoniot must have been very close to the steady-state velocities. Thick-headed projectiles were used for the Hugoniot shots and the "flat-topped" profiles measured in quartz testify to the fact that the peak pressure at the shock front was not being attenuated before transit through the target. Rarefactions from the sides of the target would also have changed the "flat-topped" appearance and would have been visible in the guarding records first.

As a basis for interpretation, smooth curves based on theoretical models and totally independent of the measured data are drawn on the same axes in Figs. 18 to 20. These smooth curves are derived from the relations of conservation of mass and momentum across a shock front (jump conditions) and take the form,

$$P = P_1 + \frac{10(u_p - u_1)^2}{V_1 - V_p}$$

where P (kbar), u_p (mm/ μ sec), and V_p (cm^3/g) are the pressure, particle velocity, and specific volume associated with the state behind the shock; and P_1 (kbar), u_1 (mm/ μ sec), and V_1 (cm^3/g) are the pressure, particle velocity, and specific volume associated with the state ahead

* See footnote on p. 1.

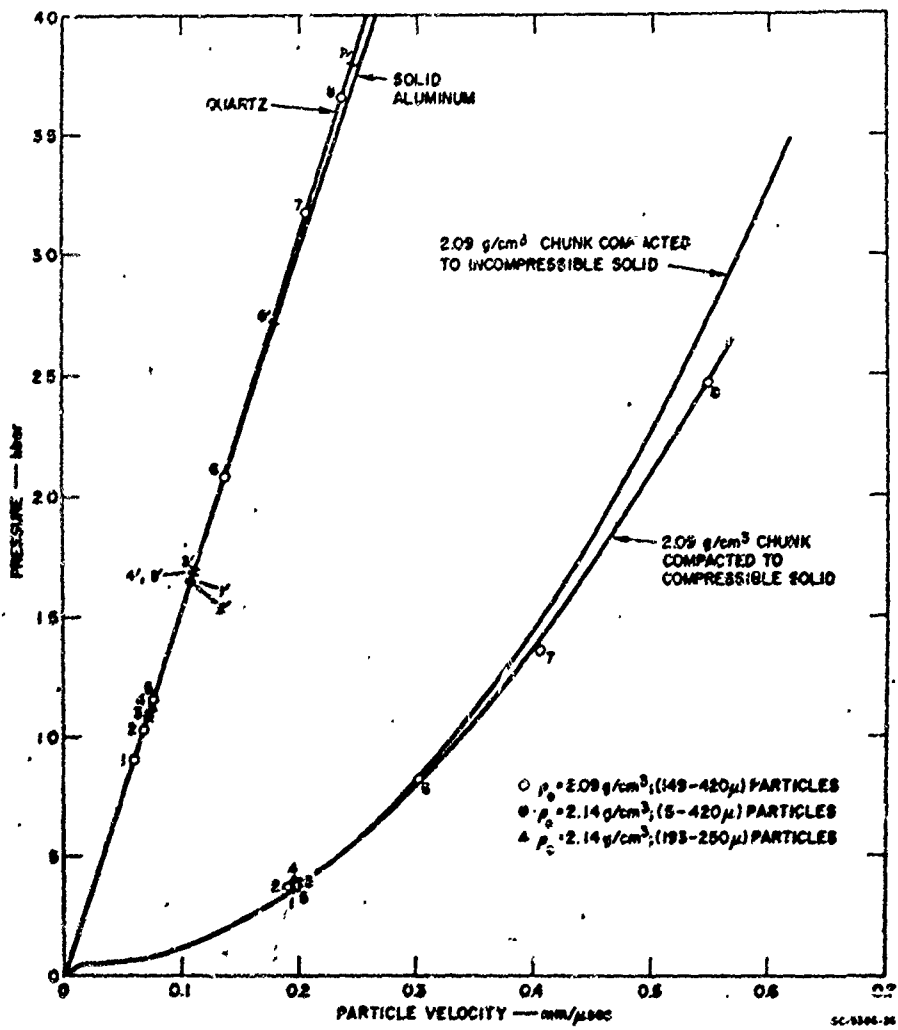


FIG. 18 PRESSURE, PARTICLE-VELOCITY DIAGRAM FOR 2.1 g/cm³ "CHUNK" ALUMINUM FOAM. Smooth curves and numbered points along quartz Hugoniot were computed as described in text.

of the shock (i.e., either the initial "rest" state or the state behind the forerunner wave, as the case may be). Curves labeled "compacted to compressible solid" were drawn using values of P , u_p , and V_p obtained from the same data used in computing Eq. (16) for solid graphite and for solid aluminum, with allowance made for any forerunner wave. For purposes of comparison the curves labeled "compacted to incompressible solid" were drawn assuming the foam to collapse to the atmospheric pressure crystal density and to remain at this density regardless of pressure (rigid locking-solid model of Fig. 1). Smooth curves are merely labeled "compacted" in cases where both types are indistinguishable for the scales employed. Values of P_1 , u_1 , and crystal density used in obtaining the curves are shown in Table III.

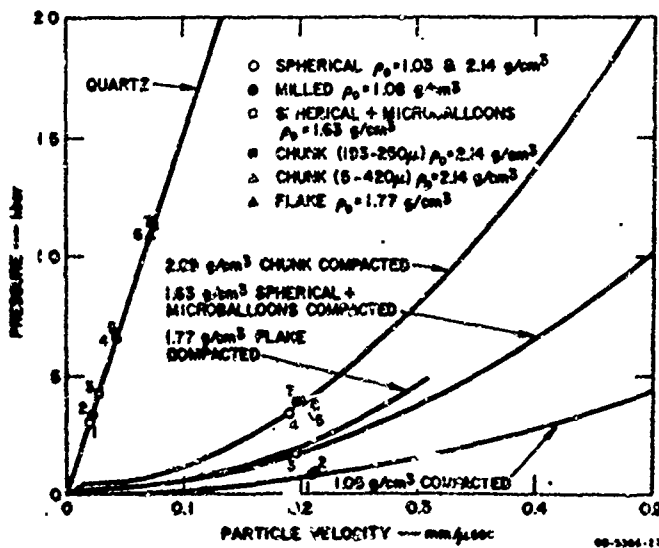


FIG. 19 PRESSURE, PARTICLE-VELOCITY DIAGRAM FOR VARIOUS ALUMINUM FOAMS. Smooth curves and numbered points along quartz Hugoniot were computed as described in text.

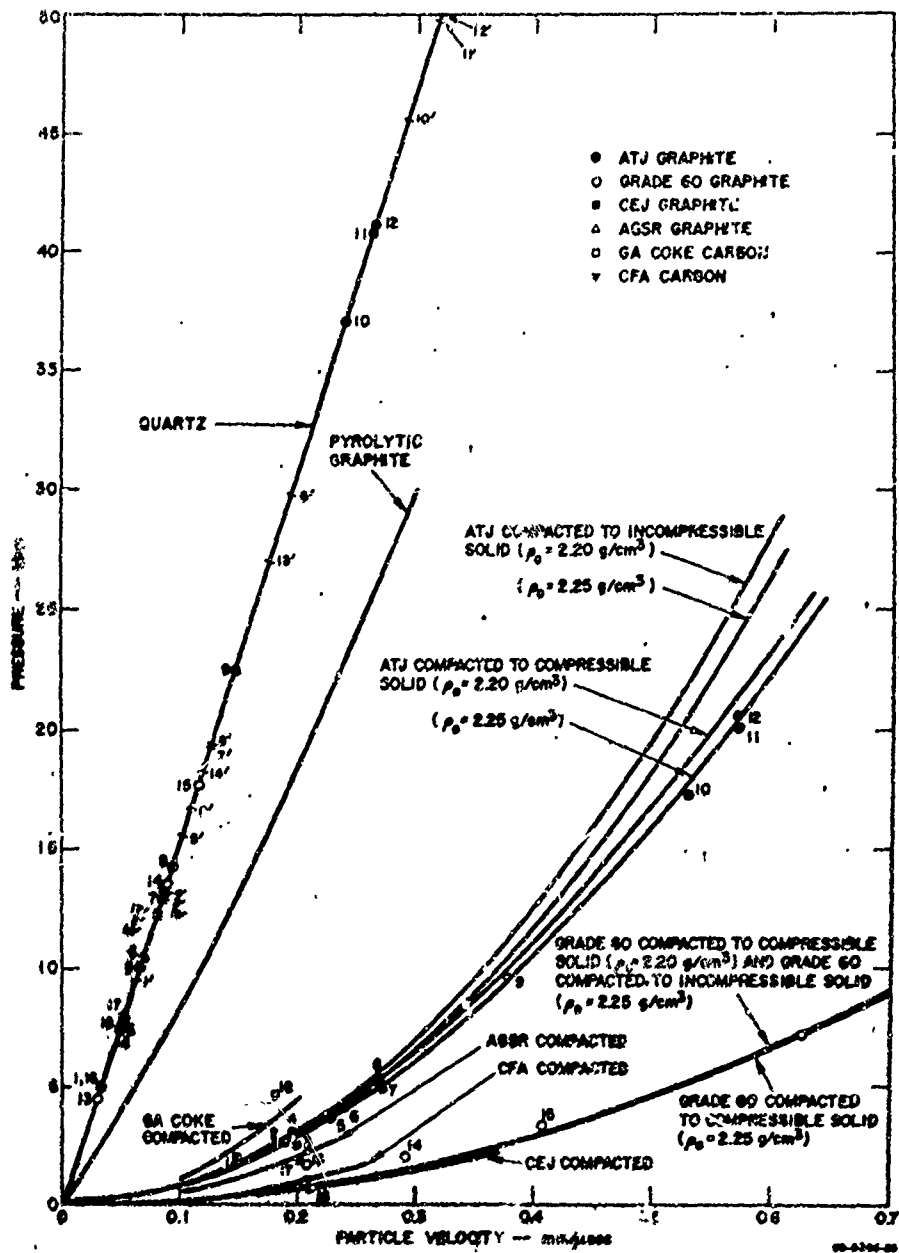
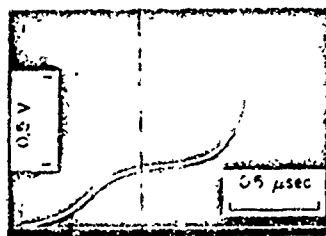
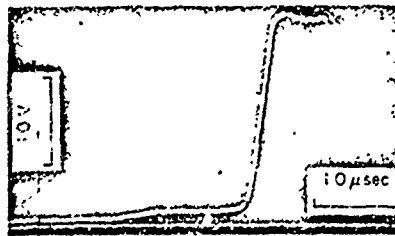


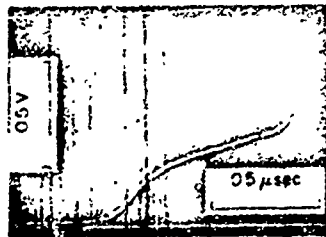
FIG. 20 PRESSURE, PARTICLE-VELOCITY DIAGRAM FOR GRAPHITE AND CARBON FOAMS. Smooth curves and numbered points along quartz Hugoniot were computed as described in text.



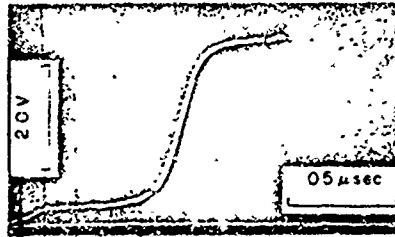
(a) SHOT NO 11,657 FORERUNNER
DETAIL IN 2.09 g/cm³ ALUMINUM
FOAM



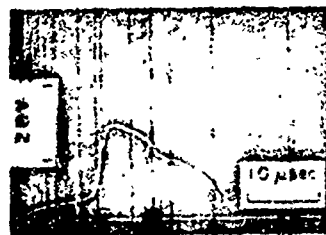
(b) SHOT NO 11,533 DOUBLE-WAVE
PROFILE IN 2.09 g/cm³ ALUMINUM
FOAM



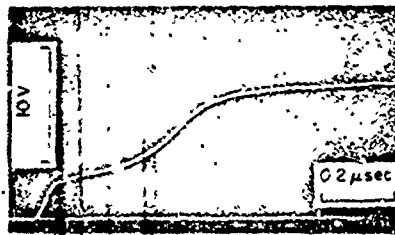
(c) SHOT NO 11,527 FORERUNNER
DETAIL IN ATJ GRAPHITE



(d) SHOT NO 11,220 DOUBLE-WAVE
PROFILE IN ATJ GRAPHITE



(e) SHOT NO 11,766 DOUBLE-WAVE
PROFILE IN ATJ GRAPHITE
ATTENUATION SHOT



(f) SHOT NO 11,118 DOUBLE-WAVE
PROFILE IN SOLID 2024-T351
ALUMINUM

FIG. 21 TYPICAL VOLTAGE-TIME PROFILES FROM QUARTZ

Voltage is related to pressure at specimen-quartz interface as described in Section V-1

Table III
 VALUES OF QUANTITIES USED IN DRAWING SMOOTH
 CURVES OF FIGURES 18 TO 20

Material	Initial Density (g/cm ³)	Forerunner		Crystal Density ^{1a} (g/cm ³)
		P ₁ (kbar)	u ₁ (mm/μsec)	
<u>Aluminum</u>				
Churk	2.09	0.45	0.015	2.71
Flake	1.77	0.0	0.0	2.71 ^a
Spherical + micro- balloons	1.83	0.1	0.004	2.71
(MD-AK) ^b	1.45	1.0	0.08	2.71
Spherical & milled	1.05	0.0	0.0	2.71
<u>Graphite</u>				
ATJ	1.72	0.33	0.01	2.20 2.25 ^c
Grade 60	1.02	0.1	0.01	2.20 2.25 ^c
AGSR	2.58	0.2	0.01	2.20
(EJ)	0.94	0.0	0.0	2.20
<u>Carbon</u>				
GA Coke	1.61	0.0	0.0	1.9 ^d
CFA	1.00	0.1	0.002	1.9 ^d

^a The value 2.7 g/cm³ may be slightly large if the wax was not completely removed during heat treatment of the flake powders (see Section IV).

^b The values for MD-AK are included here for purposes of comparison although the experimental data (see Table VII, Appendix II) did not allow precise enough measurement of Hugoniot points to require the inclusion of both curves for MD-AK in the figures.

^c The value 2.25 g/cm³ is for "good" natural graphite,¹⁸ whereas the value 2.20 g/cm³ is a typical initial density for pyrolytic graphite.¹⁹

^d This value is a reasonable density. Possible values range from 1.5 to 2.0 g/cm³.¹⁹

Reference to Figs. 18 and 20 shows that in the cases where several reliable data are available the "compacted to compressible solid" curves are essentially best-fit curves to the experimental data. This result indicates that the pressure-volume states of the foams after compaction lie indetectably close to those of the solid materials. Data points below about 2 or 3 kbar are unreliable for some materials because of uncertainties associated with the forerunner wave (see Section V-A), but have been included in the figures.

These results are reasonable for the distentions and pressures involved, in light of the discussion of Section II. There is some uncertainty introduced into the smooth curves by the extrapolation or normalization of data, and particularly in the choice of the appropriate crystal density for the graphite specimens, but the uncertainties are not large; the effect of changing the assumed density of solid graphite is illustrated in Fig. 20. The results obtained lend confidence to the assumed P-V Hugoniot of Section III, with regard to the crystal density curves GDE (Figs. 3 and 4).

A very important point is raised by the indicated cross curves in Figs. 18 to 20. Numbered points along the quartz Hugoniot correspond to pressures indicated by quartz for shots in which the foam Hugoniot point of the same number was measured. The primed points represent expected pressures in quartz for the given foam Hugoniot point on the assumption that compacted foam behaves like the initially solid material. When total compaction has occurred the compacted foam should behave like the solid material, since the results discussed above show that the P-V states of compacted foam and initially solid material lie so close together. The indications from the quartz voltages that the cross curves are considerably more shallow implies the dubious result of a compressibility for the "fully compacted" foams much greater than that

for the initially solid material, i. e., high retained porosities (generally five to ten percent) would have to be present even at the higher pressures, in contradiction with the Hugoniot measurements; furthermore, this porosity would have to be retained after one strong shock but removed after two weaker ones.

In order to clarify the situation, shots were fired using a 1/4-in.-thick 2024-T351 aluminum plate between the foam and the quartz; others were fired using Manganin gages^{17,18} in this configuration. The results of these shots showed the original quartz-inferred pressures to be in error and the assumed cross curves (primed points) to be correct. Further, shots with quartz gages on solid 2024-T351 aluminum targets indicated pressures in quartz that were in accord with the impact conditions and known Hugoniots. The obvious conclusion is that quartz responds differently when impacted by porous materials and cannot be used indiscriminately, even if the porous material fully compacts to solid density within the rise time of the shock profile. The lower readings in X-cut quartz are consistent with the piezoelectric tensor for the material. The observations about forerunner pressures in Section VI-a should not be affected, however, because adequate allowance has been made in their qualitative nature. Furthermore, errors in forerunner magnitude should have the same (small) effect on the experimental points and smooth curves of Figs. 18-20, so that the conclusions of this section (VI-3) remain unaffected.

4. Shock Attenuation Experiments and Calculations

One important goal of the research program was to develop the ability to predict the behavior of a foam subjected to short-duration, high-amplitude, impulsive loading. The flyer plate experiments described in Section V were designed to approximate such pulses with momentum densities of 0.5 to 0.75×10^6 dyne-sec/cm² (see Table IV)

Table IV
DATA FOR SPICK ATTENUATION EXPERIMENTS

Material	Description of Specimen		Shot No.	Impact Conditions			Reference Figure
	Density (g/cm ³)	Thickness (mm)		Projectile Velocity (mm/μsec)	Input Momentum Density ^a (dyne-sec/cm ²) x 10 ⁴	Shock Tilt (across Page) (μsec)	
<u>ATJ Graphite</u>	1.78	2.74	11,684	0.660	0.76	0.071	22a, 24
	1.73	4.09	11,659	0.630	0.69	0.043	22b
	1.74	2.74	11,788	0.486	0.53	0.042	22c
<u>Chumk Aluminum (149-420 μ)</u>							
	2.09	2.79	11,784	0.496	0.54	0.035	23a
	2.09	2.78	11,785	0.477	0.52	0.046	23b
	2.08	2.77	11,786	0.679	0.74	0.042	23c
	2.14	1.63	11,787	0.484	0.53	0.020	23d

^aUsing 0.0160-inch-thick 6061-T6 aluminum flyer plate ($\rho_0 = 2.698 \text{ g/cm}^3$).

delivered within less than $0.15 \mu\text{sec}$. The resulting voltage-time profiles at the quartz-foam interface were recorded.

If the quartz gage current is proportional to the stress difference between its two faces, a reasonably good idea of the pressure profile can be obtained even after a shock has transited the gage, since the gage is backed up by material of similar shock impedance. The shock transit time in the gage was $1.66 \mu\text{sec}$, so profiles were reconstructed by adding to each pressure reading the reading $1.66 \mu\text{sec}$ ahead of it. This procedure should result in computed pressures which are slightly high, due both to the action of the shock on the gage¹¹ and to the fact that the impedance of the backing material was actually slightly lower than that of quartz. On the other hand, the observations reported in Section VI-3 indicate that use of the quartz gage on porous targets may result in erroneously low pressure readings if the standard calibration (Fig. 9) is used. Therefore, the reconstructed experimental profiles (solid lines of Figs. 22 to 24) should be considered reliable as to timing and general shape, but not necessarily as to absolute pressure level. It should also be noted that profiles at times greater than about $4 \mu\text{sec}$ after impact ($t=0$ at impact) will deviate towards lower and lower pressures, due to the arrival of side rarefactions, and should therefore not be compared with the one-dimensional computer calculations.

To test our ability to predict the response of the foams, calculations were made for all profiles by using the artificial viscosity, digital computer program and equation of state information described in Section III. The computational procedure sometimes distorts the pressure at the quartz-foam interface, in which case the pressure in Zone 4 of the quartz has been used and the times have been adjusted to those at the interface by using the shock velocity in the quartz and noting that each cell is 0.008 cm wide. The resulting profiles are also plotted in Figs. 22 and 23.

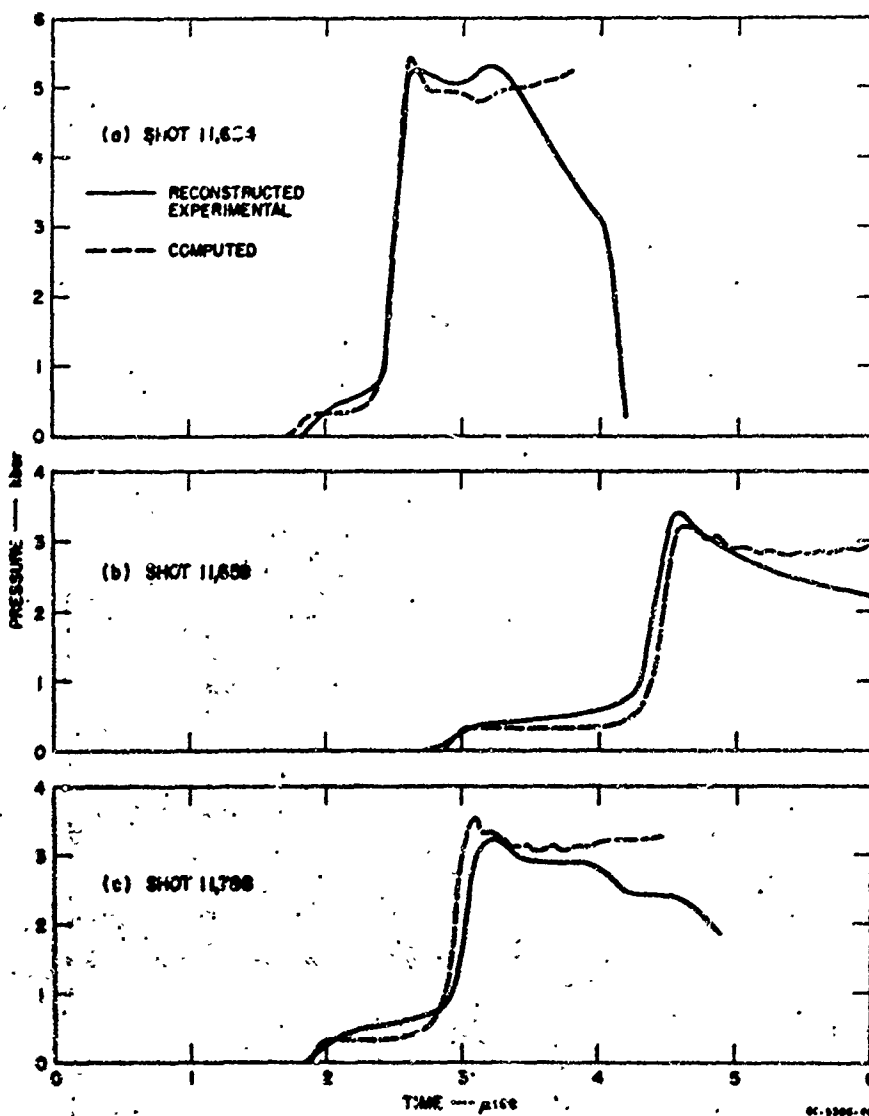


FIG. 22 RECONSTRUCTED AND COMPUTED PRESSURE-TIME PROFILES AT FOAM-QUARTZ INTERFACE FOR SHOCK ATTENUATION STUDIES
Flyer-plate impact occurs at time = 0. Foam is ATJ graphite.

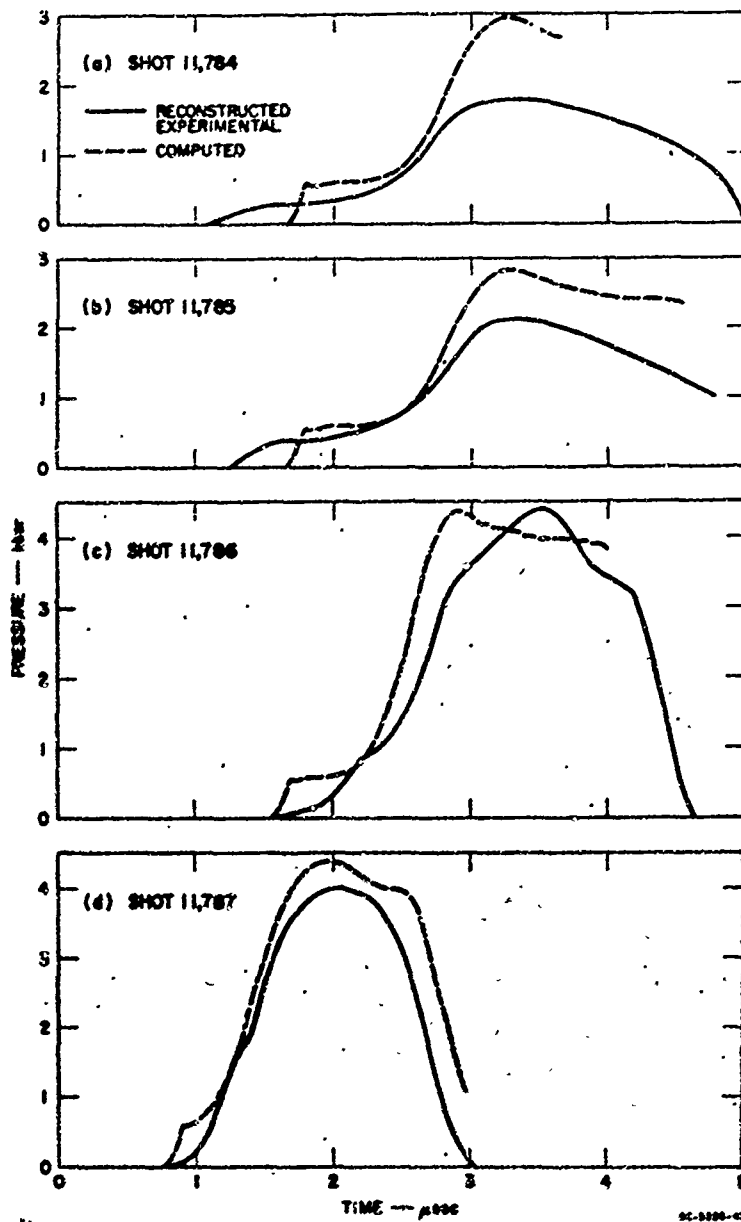


FIG. 23 RECONSTRUCTED AND COMPUTED PRESSURE-TIME PROFILES AT FOAM-QUARTZ INTERFACE FOR SHOCK ATTENUATION STUDIES
 Flyer plate impact occurs at time = 0. Foam = 2.1 g/cm^3 "chunk" alumina.

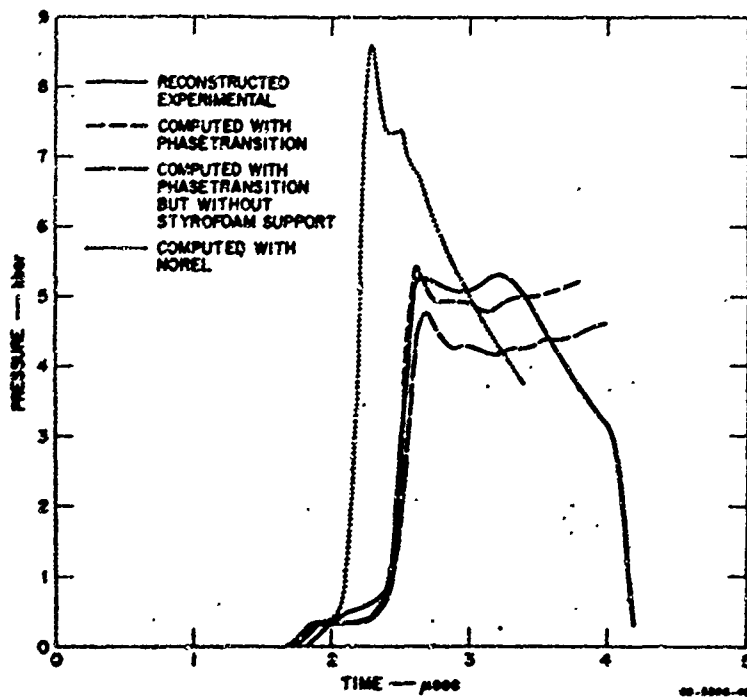


FIG. 24 RECONSTRUCTED AND COMPUTED PRESSURE-TIME PROFILES AT FOAM-QUARTZ INTERFACE, SHOWING EFFECT OF VARIATIONS IN COMPUTATIONAL PROCEDURE
Foam is ATJ graphite, Shot 11,654.

For ATJ graphite, Fig. 22 indicates that agreement between calculated and experimentally measured profiles is very good. For the aluminum foam, agreement between calculated and experimental profiles is fairly good. Presumably, agreement could be improved and certainly made more meaningful by a better knowledge of forerunner pressures and any resulting modification in the constants of Eq. (17).

It is clear that a porous solid will evidence rise times that depend upon the scale of homogeneity; i. e., a finite time is required for each particle of the foam to come into pressure and particle-velocity

equilibrium with its surroundings. On the other hand, the artificial viscosity used in the computations acts like a real viscous force against which irreversible work must be done in compressing the solid. By appropriately adjusting the value of Q , the rise times of the calculated pressure pulses can be changed, and there is a corresponding erosion of the pulse because of the additional energy dissipation. With this in mind, an attempt to match the profiles in aluminum foam was made by increasing the value C_{ona} from 0.1 to 0.5 in Eq. (11) and adjusting the values of R and K in Eq. (17). The resulting profiles were in better agreement with experiment but the introduction of a larger linear viscosity as such has not been justified on a physical basis. Further investigation of the problem, especially from a microscopic point of view, would be of considerable interest.

In order to see the effects of various assumptions, the experimental and computed profiles of Fig. 22a have been reproduced in Fig. 24, along with profiles calculated (1) neglecting the styrofoam region behind the flyer plate and (2) including the styrofoam region but using release paths for ATJ graphite coincident with the compression paths (NOREL procedure), as shown in Fig. 4 of Section III. It may be seen that the styrofoam had only a small effect and that the "spring-back" in ATJ graphite must occur at essentially zero pressure, so that the "locking" release curves are the appropriate ones to use.

In conclusion, it might be stated that while reasonably good agreement can be achieved, the shape of the P-V Hugoniot in the partially compacted region has been conveniently chosen by Eq. (17) with appropriate constants and is sensitive to errors in assumed forerunner pressures. It would also be desirable to confirm experimentally the choice of assumed release paths. Another possible source of error lies in the extrapolation and normalization of data for the solid materials. The introduction of a linear viscosity to

aid in matching wave profiles can be of value but has not been rigorously justified on physical principles. A possible refinement of the calculations would be to employ an elastoplastic model for the Hysteresis of the compacted materials.

SECTION VII

SUMMARY AND RECOMMENDATIONS FOR FURTHER WORK

A portion of the effort was directed to the development of suitable aluminum foams on which to make shock measurements. Aluminum presents a particularly formidable problem because of the omnipresent, nearly impervious, oxide layer. We have succeeded, however, in producing relatively homogeneous foams in the density range of 40 to 80 percent of crystal density. We have also successfully varied particle shape, size, and size distribution. Production techniques investigated include: (1) hot pressing of aluminum powders; (2) cold pressing and subsequent sintering of aluminum powders; and (3) repeated hot pressing and sintering of a mixture of aluminum powders and silica microballoons.

Hugoniot measurements using newly developed techniques have been made on several graphite (or carbon) and-aluminum foams. Hugoniot of one graphite and one aluminum foam (both about three-fourths of crystal density) have been traced in some detail up to about 25 kbar. Attempts have been made to determine the pressures transmitted to a quartz (or solid aluminum) structure for given pressures in the foams. We have found in general that in the pressure and porosity range studied, the "compacted" volumes for pressures above a few kilobars are essentially those of the solid materials at the same pressure.

In the case of aluminum, the foam appears to "lock" to approximately solid aluminum density and lose its foam characteristics (i. e., the density of recovered shocked foam corresponds approximately to that of solid aluminum). On the other hand, recovered shocked specimens of ATJ graphite exhibit densities very close to their initial densities (i. e., they are recovered as foams). The equation of state information outlined above is of major importance for any shock attenuation calculations.

Parameter variation studies included various particle (or pore) sizes, shapes, and distributions. In general the preliminary results indicated that these factors are probably of less importance than the strength of the solid matrix. Where the matrix is strongest the forerunner speed and amplitude may be expected to be the greatest. There is a tendency for these desirable characteristics to be associated with foams of higher density if the other factors are kept constant. With the present state of material development of foams of the type studied, there is too much scatter in forerunner characteristics to enable more specific correlations.

The artificial viscosity computer code has been successfully adapted to calculation of shock attenuation in porous solids. Within the idealizations of the models employed, calculated transit times and shock profiles are in reasonably good agreement with the experimentally measured quantities, particularly for the case of ATJ graphite. However, uncertainties in forerunner pressure and in the Hugoniot curve in the partially compacted region limit this result to a demonstration of capability rather than providing a definite numerical result.

During the course of the work several topics have suggested themselves as important areas for further research:

1. Precise measurement of forerunner pressures (e. g., by using an aluminum witness plate between the foam and a quartz gage) and of pressure-time profiles for attenuation shots should be made so that the actual attenuation profiles can be established and checked against the artificial viscosity calculations.
2. Research on new materials such as heavy metal foams and ceramic foams should be initiated.
3. The study of pertinent structural variables controlling the forerunner speed and amplitude should be extended and expanded.

Correlations with various static and quasi-static measurements should continue to be investigated.

4. Optimum distention ratios for a given material should be established. This optimum ratio will depend upon the type of foam, but for a given foam it will involve a compromise between the large forerunner amplitude (and speed) associated with low distentions and the rapid "attenuation from the rear" associated with higher distentions.

5. Hugoniot measurements should be extended to wider porosity ranges, and an attempt should be made to obtain reliable data at pressures just greater than that of the forerunner wave. A knowledge of the actual pressures required for complete compaction is very important for the calculations of shock attenuation. At present we can assign upper and lower bounds to these values for graphite and aluminum but we do not have a direct measure of the P-V curve between elastic and compacted segments.

6. Hugoniots for aluminum foams with different particle sizes and shapes have been found to essentially coincide at about 4 kbar, but the work should be extended to other materials and to higher pressures where any differences might be more easily observed.

7. The release curves, especially in partially compacted regions, are of major importance. It is also clear that the release curves for compacted graphite are not simple locked curves, but the way in which they deviate from the locked model has only been inferred, and has not been experimentally measured. Attempts should be made to measure release curves directly.

8. A basic inquiry as to why some foams (like aluminum) essentially lock, and others (like graphite) do not, would be of considerable interest. It would further be of interest to discover whether a shocked foam which does not lock may act as an effective countermeasure material in case of subsequent "hits." Investigation of release curves

may shed some light, but experiments designed so that specimens with a well known history can be recovered intact for detailed study and perhaps subsequent shocking would be valuable.

9. Accurate Hugoniot for the solid materials should be measured at low pressures in order to eliminate the uncertainties associated with extrapolation and normalization of data. The elastic-plastic model should then be used in the computer calculations.

10. Investigation of dissipative processes in foams should be conducted from a microscopic viewpoint to lead to a better understanding of wave profiles.

APPENDIX I

DESCRIPTION OF CALCULATION ROUTINE USING THE ARTIFICIAL VISCOSITY CODE

A. Essential Steps

The essential steps in the calculation are summarized below:

1. Read in: Material constants, number of regions, dimension and kind of material in each region, number of cells in each region, geometry (plane, cylindrical, or spherical), Q -constants, control instructions for printing output, flyer plate velocity.
2. Determine cell size in each region.
3. Set initial conditions for each cell: mass in each cell, Euler coordinate of each cell.
4. Begin computation.
5. Calculate new particle velocity for each cell from momentum equation.
6. Calculate new Euler coordinate for each cell.
7. Calculate new specific volume from continuity equation.
8. Calculate new Q for each cell.
9. Calculate new P for each cell.
10. Calculate Δt for next time step.
11. Print results.
12. Return to step 5 and repeat. Continue cycling until problem is complete.

Both the initializing (Step 3) and the computation of P (Step 9) are accomplished in procedures. The initializing is straightforward; the computation of P requires iteration if the constitutive relation is energy-dependent. If it is not energy-dependent, it is computed directly from the specific volume previously determined. The entire program as used in a typical run is reproduced at the end of this appendix.

B. Zoning

The experimental configuration is described in Section V. Briefly, it is a one-dimensional experiment which consists of a flyer plate assembly (a 6061-T6 aluminum flyer plate backed by a 2 lb/ft³ styro-foam support) impacting the target (foam) which is bounded on the opposite side by quartz.

Computation is started at the instant the flyer plate strikes the target. Initial values are: pressure $P = 0$ everywhere; particle velocity $u = u_1$ constant in flyer plate assembly; $u = 0$ elsewhere; specific volume has its zero pressure value, $V = V_0$ everywhere. Artificial viscosity Q is zero everywhere. A value of the time increment Δt (DELTA)* must be specified in the input for the first cycle. Care must be taken that this not be too large. If it is, a pressure spike is produced at the flyer plate/specimen interface, which causes a wildly fluctuating output.

The number of zones in each region can be specified somewhat at will; however, fluctuations in the output are reduced by choosing zone size for each region in such a way that the minimum Δt (TLIMA) for each region has about the same value. Zone size is calculated as initial region thickness divided by number of zones in region (under SAMES); here, too, reference is made to procedures ZSOLID and ZWATER, in which initial values are set.

Geometry is made planar by setting $ALP = 1$ under LISTMTLS

A logical variable is set $PUP [J] = TRUE$; its use is described in Section D of this appendix.

C. Computing Steps

The computation for a given cycle starts at LEFT: PPEAK = 0, etc. At this point all parameters for the previous cycle (time = t) have been determined, t has been advanced to $t + \Delta t$, and cycle to cycle + 1.

* Labels and names of variables and procedures have reference to the ALGOL program used for the computations.

Computations are made in the following order:

U[1] is a new value for particle velocity in the first zone,

J = 1.

XA is temporary storage for the value of the Euler coordinate of the Jth zone.

U[J1] is the new value of U for the (J + 1) zone.

X[J] is the Euler coordinate.

VN is the new value of specific volume for zone J.

QA is the new value for stress from artificial viscosity.

New values of P[J], E[J] are calculated in the procedures styrofoam, ELASTOPLASTIC, WATER, or PHASETRANSITION; the procedure entered at this point depends upon the value of the parameter BURN[S], which has previously been prescribed for each of the four regions: S = 1 (styrofoam support), S = 2 (aluminum flyer plate), S = 3 (target), S = 4 (quartz); i. e.,

BURN[1] = 5

BURN[2] = 0

BURN[3] = 4

BURN[4] = 3

Following the calculation of P[J], the variable V[J] is replaced by the number temporarily stored in VN, and J is tested to see whether it is beyond the shock front. If it is not (FALSE), another J-cycle is made in response to the instruction "IF J < JSTAR+1 THEN GO TO GETUV." If it is (TRUE), a new Δt is determined; the information stored for the past cycle is printed (if desired), and a new time cycle is started by the last instruction of the program, "GO TO LEFT."

D. Comments on PHASETRANSITION Procedure

The implementation of the prescription for calculating P and V (see Section III-D) is simple:

$$\Delta V = V(J, t + \Delta t) - V(J, t)$$

can be stored, and as long as it is negative, compression of that zone is occurring. When it turns positive, expansion has started.

Although we have not found it to be the case so far, it is possible that fluctuations inherent in the numerical integration may cause difficulties with this simple criterion. To protect against that eventuality if it should arise in the future, a routine has been included in the program to smooth out the effects of fluctuations in the sign of ΔV . The disadvantage of its use is the resulting delay in changes between compression and rarefaction, so it is recommended that the value of n (see below) be kept as small as possible. We have used $m=1$ (which corresponds to the simple criterion above) in all cases.

Routine to Check for Compression or Rarefaction. Running average values of V and of ΔV could be carried along and these should have sufficient stability to serve as controls. The normal definition of a running average over an interval $(t-\tau)$ to t can be written

$$\bar{V}^R(t, \tau) = \frac{1}{\tau} \int_{t-\tau}^t V(t) dt$$

or:

$$\bar{V}^R(t_N, m) = \frac{1}{m} \sum_{n=N-m}^N V(t_n) \quad (25)$$

or:

$$\bar{V}^R(t_N, m) = \bar{V}^R(t_{N-1}) + \left[\frac{V(t_{N-m-1}) + V(t_N)}{m} \right] \quad (26)$$

If this were carried in the present computation, it would require that values of $P[J]$ for the previous m cycles be stored. In order to conserve storage, define a quantity

$$\bar{V}(t_N, m) = \left(\frac{m-1}{m} \right) \bar{V}(t_{N-1}) + V \frac{(t_N)}{m} \quad (27)$$

If we denote

$V(t_N)$ by V_N^R , etc., Eqs. (26) and (27) can be written

$$V_N^R - V_{N-1}^R = \frac{V_N - V_{N-m}}{m} \quad (28)$$

and

$$V_N - V_{N-1} = \frac{V_N - V_{N-1}}{m} \quad (29)$$

Then if V passes through a minimum, V^R passes through a minimum somewhat later. But, unless changes have been very rapid, $V_{N-1} < V_{N-m}$; so V passes through its minimum after V and before V^R . Consequently, it should serve as an adequate monitor for changes between compression and rarefaction if m is chosen properly.

The monitoring function of V is fulfilled by using V to determine a reference "turnaround" volume, V_c , such that whenever $V > V_c$, the state point is assumed to lie on a reversible curve, CF of Fig. 3; and the function describing these curves is $f_{int}(V)$, given by Eqs. (18) and (20). The initial elastic curve, AB, of Fig. 3, is thus included in $f_{int}(V)$. If V is ever $\leq V_2$, it is assumed that the material is locked into its solid state, and all subsequent compression and expansion will take place along the curve $f_3(V)$ given by Eq. (18). Thus, for each cycle the function of the machine is to:

- 1) Calculate new V and ΔV .
- 2) If new $V \leq V_c$, then calculate $P = f_1(V)$ or $f_2(V)$ or $f_3(V)$ and return to main program
- 3) If new $V > V_c$, then set V_c , P_c and V_{c0} ; calculate $P = f_{int}(V)$; and return to main program.

The information stored in the memory at the time of entering the procedure, (with definition of symbols) is:

$PUP[J] = \text{TRUE or FALSE}$. If TRUE, $P = f_1(V)$ or $f_2(V)$ or $f_3(V)$. If FALSE, $P = f_{int}(V)$.

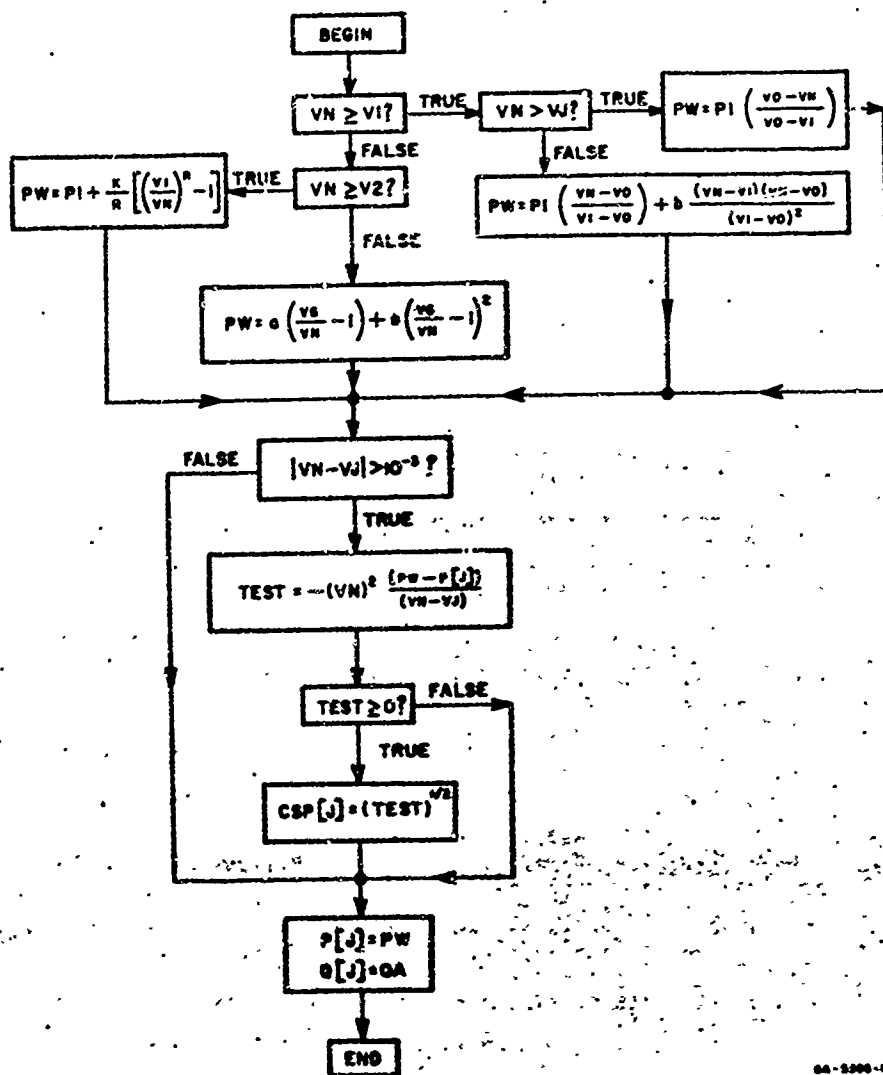
INT[J] = TRUE or FALSE. If TRUE, VC, PC and VCO have not been set. If FALSE, they have been set.
P[J] = P(J,N-1) = previous value of P
VBAR[J] = $\bar{V}(J, N-2)$
PC[J] = $P_c(J)$
VC[J] = $V_c(J)$
VCO[J] = $V_{co}(J)$
MM = m = number of values of V in F
VN = V(J, N), the current value of V to be used in computing the new pressure.

Parameters to be determined in the procedure are:

VBARA = $\bar{F}(J, N-1)$ and VC[J], PC[J], VCO[J] if F turns around
PW = new value of P = P(J, N)
PUP[J]
INT[K]

E. Comments on NOREL Procedure

The NOREL procedure is very simple. A flow chart is shown in Fig. 25, since the procedure does not appear in the program listing in Section F of this appendix.



GA-5000-10

FIG. 25 FLOW CHART FOR MOREL PROCEDURE

F. LISTING OF COMPUTER PROGRAM

```

BEGIN
FILE RIN (3,10); POUT 4(3,15);
INTEGER NUM; LABEL FINISH;
HEAD(RIN,/,NUM);
NUM = NUM + 10;
BEGIN
INTEGER COUNT,COUNTS,CYCLE,CYCLES,HALT,J,J1,JC,JCC,JCRIT,JMAX,RESTART,
JPMAX,JSTAR,JT,NT,NTT,OPTION,S,S0,S1,EF,
SP,I,JPB,JPE,ALP,RR;
REAL CONA,CQ,CQSQ,CQSQ,DELT,DELTI,DELU,DELX,DEMU,DL,
DL1,DM,DPOMU,DTMX,DTN,DTNH1,QA,JMAXF,
LEFTP,LINEAR,LX,M,M1,MUN,PE1,PF,PH,PLEFT,PMAX,PMIN,PPEAK,
PSCALE,TAU,TIMES,TLIMB,TQUIT,UO,
Z,PW,EW,FW,EA,EJ,VJ,BB,TEST,P11,V11,KK,
C,PS,CSPE,VN,X0,YE1,YF,YPM,XA,XSPA,VR ;
INTEGER ARRAY CELLC(25),BURN,HC(9);
REAL ARRAY A,B,C,DX,G,MUA,MY,PA,PHA,RHO,VO,Y,DV,GAM,VCJ,L(0:5),
AA(0:5),TW(0:25),E,F,MU2,MUF,P,PE,Q,TMP,EI,PI,X,
XALPS,ENT,CSP,TB,TLIMA,U,YP, VC(0:NUM);
BOOLEAN BOOL;
COMMENT PHASETRANSITION VARIABLES; INTEGER MM; REAL V1,P1,V2,P2,V0,V6,K,R;
REAL VBARA,DVBARA;
REAL ARRAY VBAR,DVBAR,VC,PC,VC(0:NUM);
BOOLEAN ARRAY PUP,INTC(0:NUM);

FORMAT FMTD(X10,"TIME =",E14.8,X4,"DELT =",E14.8,X4,"DTN =",E14.8,X4,
"CYCLE =",I5,X4,"JCRIT =",I5,/) ;
GTAG(X2,"J",X8,"U",X11,"V",X11,"P",X11,"E",X11,"O",X11,
"X",X10,"MUE",X9,"MUF",X3,"TLIMA",//);
F3(I3,8F12.6,E13.5) ;
F1(X6,"ALP",X10,"DELT",X11,"DTMX",X11,"CONA",X13,"CQ",/,I8,X7,
4E15.6,//);
FK("CYCLES COUNTS NTT",X6,"TW(L)",/,3I6,X2,10F10.3,/,10(X20,
10F10.3,//),/);
FBURN(I10,"REGIONS",9I5,//);
F0(X8,"A",X11,"B",X11,"C",X11,"G",X10,"MUA",X10,"PA",X10,"MY",
X10,"RHO",X8,"M",X11,"L"),
F2(8F12.4,I8,X4,F12.4,//);
MPH(X4,"M",X5,"R",X6,"V1",X11,"P1",X11,"V2",X11,"P2",X11,"V0",X11
,"V6",X11,"K",X10,"H",X5,"L",/,2I6,7F13.6,I6,F11.6,//);
HQ(X7,"V0",X9,"M",X5,"L",/,F13.6,I6,F11.6,//);
FPU(//,X10,"TAU",X15,"LEFTP",X16,"UE1",X9,"OPTION",/,
3E20.8,I5,//);
FSUR("TIME =",E14.8,X4,"UFS =",E14.8,X4,"XFS =",E14.8,X4,
"CYCLE =",I4,X3,"JPMAX =",I4,X3,"JCRIT =",I4,/) ;
FOAGE(I4,5F15.8);

LIST INTERVAL(TIMES,DELT,DTN,CYCLE,JCRIT);
EDGE(J,UEJ),X(J));
MTLS (ALP,DELT,DTMX,CQ(A,CQ) ;
CONTROL(CYCLES,COUNTS,NTT,FOR NT+1 STEP 1 UNTIL NTT DO TW(NT));
STREAMLINE(JCC,FOR JC+1 STEP 1 UNTIL JCC DO CELLC(JC));

```

```

REGIONS (S1, FOR S = 1 STEP 1 UNTIL S1 DO BURNES)
EQST(A(S), B(S), C(S), G(S), MU(A(S), P(A(S), Y(S), RHO(S), H(S), L(S)),
PHASE(MM, R, V1, P1, V2, P2, V0, V6, K, H(S), L(S)),
QUARTZ(VOL(S), H(S), L(S)),
PULSE(TAU, LEFT, UE1), OPTION),
ARRAYS(J, UE(J), VE(J), PE(J), EE(J), QE(J), XE(J), MUE(J), MUF(J), TLIMAJ),
FACE(TIMES, UE(J), XE(J), CYCLE, JPMAX, JCRIT),
FORGAGE(J, UE(J+1), VE(J), PE(J), QE(J), XE(J+1)),
LABEL READING, LEFT, SETJ, ULEFT, GETUV, GETX, FLAP, NEWT)

```

```

PROCEDURE ZWATER : BEGIN

```

```

  CSPS = 0.3 ;
  BB = 0.1 ;
  FOR J = (H(S)-1) + 1 STEP 1 UNTIL H(S) DO BEGIN
    VL(J) = VOL(S) ;
    XE(J+1) = XE(J) + DX(S) ;
    XALP(S(J) + (XE(J+1) + ALP - XE(J) + ALP) / VE(J) ;
    UE(J+1) = QE(J) + 0.0 ;
    PE(J) = 0.0 ;
    TLIMAJ = DELT ;
    CSPE(J) = CSPS ;
    VBARE(J) = V0 ;
    PUPC(J) = INTC(J) = TRUE ;
  END ;
END ZWATER ;

```

```

PROCEDURE WATER :
COMMENT QUARTZ REPLACES WATER :
BEGIN

```

```

  PE(J) = .869 * (1.0 - 2.65 * VN) ;
  CSPE(J) = .5728 ;
  QE(J) = 0A1 ;
END WATER ;

```

```

PROCEDURE STYROFOAM :

```

```

BEGIN
  IF VN > 31.25 THEN BEGIN VN = 31.25 ; PH = 0.0 ; END ;
  IF 31.25 < VN AND VN < 94.221 THEN PH = (31.25 - VN) / (31.25 - 94.221) * 0 - 3
    * (1.0 - .1 * (VN - 94.221) / (31.25 - 94.221)) ;
  IF VN < 94.221 THEN PH = (.090478 + .200167 * (.9524 / VN - 1)) * (.9524 / VN - 1) ;
  PE(J) = PH ;
  QE(J) = 0A1 ;
  CSPE(J) = .4 ;
END STYROFOAM ;

```

```

PROCEDURE ZSOLID : BEGIN

```

```

  VOL(S) = 1.0 / RHO(S) ;
  CSPS = SORT ((1.0 + 4.0 * Q(S) / 3.0) * VG(S) * A(S)) ;
  FOR J = (H(S)-1) + 1 STEP 1 UNTIL H(S) DO BEGIN
    VL(J) = VOL(S) ;
    XE(J+1) = XE(J) + DX(S) ;
    XALP(S(J) + (XE(J+1) + ALP - XE(J) + ALP) / VE(J) ;
    UE(J+1) = PE(J) + QE(J) + 0 ;
    MUF(J) = -0.0001 ;
    MUE(J) = MU(A(S)) ;
    PE(J) = PH(A(S)) ;
  END ;

```

```

YPCJJ = YESJ ;
TLIMALJJ = DELT ;
CSPCJJ = CSPS ;
EIJJ = 0.0 ;
END END ZSOLID ;

PROCEDURE PHASETRANSITION;
BEGIN
FORMAT F7(9(F11.6,X2));
LABEL RESET;
VBARA:=(MM-1)*VBAREJJ+VN)/MM;
UVBARA:=VBARA - VBAREJJ;
IF NOT PUPCJJ THEN IF VNSVCEJJ OR VCLJ=0 THEN PUPCJJ = INTEJJ = TRUE;
IF PUPCJJ THEN IF VBARA > VBAREJJ THEN PUPCJJ = FALSE;
IF PUPCJJ THEN BEGIN
IF V1 SVN THEN BEGIN
Pw=P1*(1.0+BB*(VN-V1)/(V1-V0))*(VN-V0)/(V1-V0);
GO TO RESET; END;
IF VN2 V2 THEN BEGIN
Pw = P1 + K*((V1/VN)*R -1)/R;
GO TO RESET; END;
END;
IF VNKV2 THEN BEGIN Pw=(.19272 +2.85475*(V6/VN-1))*(V6/VN-1);
COMMENT THIS EQUATION IS FOR GRAPHITE, FOR ALUMINUM SUBSTITUTE
Pw = (.72922 + 1.71742*(V6/VN -1))*(V6/VN -1);
GO TO RESET; END;
IF (UVBARAJK0 AND INTLJJ) OR VJSV2 THEN BEGIN PCCJJ:=PCJJ; VCCJJ:=VCEJJ;
IF VJKV2 THEN VCCJJ = V2;
VCOEJJ = V0 + (V6-V0)*(VCEJJ-V1)/(V2-V1); INTEJJ := FALSE;
END;
IF VCLJJ=VCOEJJ THEN
BEGIN WRITE(POUT,F7,J,VCEJJ,VCOEJJ,VN);GO TO RESET;END;
IF VN>VCOEJJ THEN VN = VCOEJJ;
Pw=PCCJJ*(1+(VN-VCCJJ)*(1+.1)*(VN-VCOEJJ)/(VCEJJ-VCOEJJ)/(VCEJJ-VCOEJJ
2));
IF Pw0 THEN BEGIN Pw=0.0; VN = VCOEJJ; END;
RESET;
IF ABS(VN-VJJ)>3 THEN BEGIN
TEST = -(VN-2)*(Pw-PCJJ)/(VN-VJJ);
IF TEST 2 0 THEN CSPCJJ = SORT(TEST); END;
VBAREJJ = VBARA; PCJJ = Pw; CEJJ=0A; DVBARCJJ := DVBARA;
END PHASETRANSITION;

PROCEDURE ELASTOPLASTIC;
BEGIN
LABEL GETM,CALCM,RETURN;
CEJJ = 0A;
MUN=(VOESJ/VN)-1.0;
DPMU=MUN*(2.0*BCS)+3.0*CCS)*MUN)+AES;
CSPCJJ= SORT((1.0+4.0*CCS)/3.0)*VOES)*DPMU);
Pw=MUN*(MUN*(CCS)*MUN+BCS)+AES);
IF (MUN#MUEJJ) AND (MUN#MUFJJ) THEN BEGIN
PCJJ=(2.0*YPCJJ)-4.0*CCS)*PELJJ+Pw*(4.0*CCS)+3.0)/3.0;
GO TO RETURN END;
YPCJJ=MYCS)*(Pw-PHALJJ)+YESJ;

```

```

IF MUN<MUFLJ) THEN BEGIN
  MUFLJ)=M1+MUN; M=0.01+M1; DL1=-YPH/G(S);
GETM: PE1=MX(M*(C(S)*M+B(S))+A(S));
  YE1=MY(S)*(PE1-PHA(S))+Y(S);
  DL=-((YE1+YPH)/G(S))*0.5-PH+PE1;
  DM=((M1-M)/(DL1-DL))*DL;
  M1>M; DL1=DL; M=M-DM;
  IF ABS(DM/M1)>1.0E-5 THEN GO TO GETM;
  MUELJ)=M; PELJ)=(-2.0*YPH/3.0)+PH;
  PELJ)=PE1; YPIJ)=YE1; GO TO RETURN END;
COMMENT MUN IS GREATER THAN MUELJ. GET VALUE OF MUFLJ);
  MUELJ)=M1+MUN; PELJ)=PH; YPIJ)=YPH;
  PLJ)=(2.0*YPH/3.0)+PH; M=0.01+M1; DL1=YPH/G(S);
CALCM: PF=MX(M*(C(S)*M+B(S))+A(S));
  YF=MY(S)*(PF-PHA(S))+Y(S);
  DL=0.5*(YPH+YF)/G(S)+PF-PH;
  DM=((M1-M)/(DL1-DL))*DL;
  M1>M; DL1=DL; M=M-DM;
  IF ABS(DM/M1)>1.0E-5 THEN GO TO CALCM;
  MUFLJ)=M;
RETURN: END ELASTOPLASTIC;

```

```

NESTART =0;          BOOL = FALSE;
  READ(RIN,/,MTLS)[FINISH];
HEADING:
  IF BOOL THEN BEGIN ALP:=AAL1;DELT:=AAE2;DTMX:=AAE3;CONA:=AAE4;
    CO:=AAE5;END;
  WRITE(POUT,PAGE); WRITE(POUT,F1,MTLS);
  READ(RIN,/,CONTROL);
  WRITE(POUT,FK,CONTROL);
  READ(RIN,/,STREAMLINE);
COMMENT NT MUST BE SET TO 1 SO RESTART WILL WORK;
  NT = 1;
COMMENT IF RESTART = 1 GO TO LEFT FOR CONTINUATION OF RUN;
  READ (RIN,/,REGIONS);
  WRITE (POUT,DL,FURN,REGIONS);
  XL1 = 0;
  HE0 = 0;
BEGIN LABEL BOTTC, SAMES, LAST, NEXT;
FOR S = 1 STEP 1 UNTIL S1 DO BEGIN
SAMES:
  IF BURN(S) = 0 THEN BEGIN
    READ(RIN,/,EBST);
    DK(S) = L(S) / H(S);
    H(S) = H(S) + H(S)-1;
COMMENT PA IS STRESS AT YIELD. PHA IS STRESS ON HYDROSTATIC CURVE AT
SAME STRAIN AS FOR PA;
    Y(S)=2.0*G(S)*PA(S)/(1.0+4.0*G(S)/3.0); PHA(S)=0.5*MY(S)/G(S);
    WRITE(POUT,F3);
    WRITE(POUT,F2, EBST);
  2SOLID : GO TO BOTTC : END;
  IF BURN(S) = 1 THEN BEGIN

```

```

READ (RIN,/, QUARTZ);
DX(S) = LCS / HCS;
HLS = HCS + HCS-1;
WRITE(POUT, HQ, QUARTZ);
ZWATER : GO TO BOTTOM; END;
IF BURNS = 4 THEN BEGIN
  READ (RIN,/, PHASE);
  VCS:=V0;
  DX(S) = LCS / HCS;
  HLS = HCS + HCS-1;
  WRITE(POUT, MPH, PHASE);
  ZWATER : GO TO BOTTOM; END;
IF BURNS = 5 THEN BEGIN
  READ(RIN,/, LCS, HCS);
  DX(S) = LCS/HCS;
  HCS = HCS + HCS-1;
  VOLS = 31.25;
  ZWATER : GO TO BOTTOM; END;
BOTTOM : END;
V(I) = P(I) + Q(I) + R(I) + S(I) + T(I) + U(I) + V(I) + W(I) + X(I) + Y(I) + Z(I);
READ (RIN,/, PULSE);
WRITE(POUT, FRU, PULSE);
READ(RIN,/, FOR I:=1 STEP 1 UNTIL 5 DO A(I));
GO TO NEXT;
LAST: BOOL:=TRUE;
NEXT:
  CLOSE (RIN, RELEASE);
FOR S = 1 STEP 1 UNTIL S1 DO IF BURNS=0 THEN EF=HCS;
IF UC1 = 0 THEN BEGIN JSTAR = HCS + 2;
FOR J = 1 STEP 1 UNTIL EF DO BEGIN
  UC(J) = UC1; END; UC(J) = 3.5 * UC(J); END
ELSE BEGIN
  IF ALP = 1 THEN
    UC1 = DVC1 / (RMC1 + 1.0); JSTAR = 3; END;
COMMENT IF INTERFACE VELOCITY DIFFERS FROM PLATE VELOCITY SET UC(J) TO
  PROPER VALUE HERE;
WRITE(POUT, QTAB);
FOR J = 1 STEP 1 UNTIL (HCS+2) DO
  WRITE(POUT, P, ARRAYS);
FOR S=1 STEP 1 UNTIL S1 DO
  FOR J = (HCS-1) STEP 1 UNTIL (HCS+2) DO
    WRITE(POUT, P, ARRAYS);
WRITE(POUT, PAGE3);
CNSO=C0+2; C0=4.0; CNSO; LINEAR=1.0; CONA+CONA;
TIMES=CYLE+CRIT;
DTN=DELTA; DELTA=DELTA; TOUT=ABS(TMENT);
END;
LEFT: WPEAK=0; TLIM=1.0; TIMES=TIMES+DELTA; CYLE=CYLE+1;
SETJ: J=5+1; J1=J+1; JT=J1+1; PLEFT=0;
LEFT: IF ALP = 1 THEN BEGIN
  ML1 = ((P1)+HCS) - PLEFT / (HCS-HCS) * V(I) * DELTA * UC1; END;
KA = UC1 * DELTA * HCS;

```

```

GETUV :
  IF J > HCSJ THEN S = S + 1 ;
  DENU = (XCJTJ - XCJ1J) / VCJ1J + (XCJ1J - XCJ3J) / VCJ3J ;
  UCJ1J = (DELTI * (PCJ1J - PCJ3J) + QCJ1J - QCJ3J) / DENU + UCJ1J ;

GETX :
  XC(J) = XA ;
  XA = DELT * UCJ1J + XCJ1J ;
  IF J = HCSJ THEN XCJ1J = XA ;
  IF ABS(UCJ1J) < 5.0E-5 THEN UCJ1J = 0 ;
  VN = (XA * ALP - XCJ1J) * ALP / XALPSEJ1 ;
  DELU = UCJ1J - UCJ3J ;
  DELX = XA - XCJ3J ;

COMMENT GET Q FOR SHOCK ;
  QA = -DELU * (CQSQ * ABS(DELU) + CONA * CSPECJ) / VN ;
  IF QA < 0 AND (CYCLE < 10 OR BURNSJ = 1) THEN QA = 0.0 ;
  TLIMAJ1J = DELX / (LINEAR * CSPECJ + CQSQ * ABS(DELU)) ;

  IF BURNSJ = 0 THEN ELASTOPLASTIC ;
  IF BURNSJ = 3 THEN BEGIN EJ = ELJ ; VJ = VCJ1J ;
  AFTER 1 END ;
  IF BURNSJ = 4 THEN BEGIN VJ = VCJ1J ; PHASETRANSITION ; END ;
  IF BURNSJ = 5 THEN STYROFOAM ;

  IF ABS(PCJ1J) < 1.0E-5 THEN PCJ1J = 0 ;
  VJ1J = VN ;
  IF TLIMAJ1J < TLIMB THEN BEGIN
  JCRIT = J1 ; TLIMB = TLIMAJ1J ; END ;
  IF (PCJ1J + QCJ1J) > PPEAK THEN BEGIN
  PPEAK = (PCJ1J + QCJ1J) ; JPMAX = J1 ; END ;
  J = J + 1 ; J1 = J + 1 ; JT = J1 + 1 ;
  IF JPHCS1J > 1 THEN BEGIN
  IF JKJSTAR + 1 THEN GO TO GETUV ;

COMMENT TEST VELOCITY JUST CALCULATED ;
  IF UCJSTAR + 1 > 0 THEN JSTAR = JSTAR + 1 END ELSE BEGIN
  IF (CYCLE MOD 10) = 0 THEN
  WRITE (POUT, F$UR, F$AGE) END ;

  IF PCCELLJCCJ = 0 AND JSTAR > CELLJCCJ + 2 THEN BEGIN
  JPB = 1 ; JPE = JSTAR + 2 ; RESTART = 1 ;
  IF BUOL THEN GO TO FINISH ELSE GO TO READING ; END ;
  IF TIME > ABS(TWINTJ) THEN BEGIN
  FLAP : JPB = 1 ; JPE = JSTAR + 2 ;
  END ;
  IF (CYCLE MOD 10) = 0 THEN BEGIN
  WRITE (POUT, DBLJ) ;
  WRITE (POUT, DBLJ) ;
  WRITE (POUT, F2, TIME(2) / 60, JSTAR) ;
  J = 1 ; WRITE (PCUT, F$UR, F$AGE) ;
  J = JPMAX ; WRITE (POUT, F3, ARRAYS) ;
  FOR JC = 1 STEP 1 UNTIL JCC DO BEGIN
  IF J > JSTAR THEN GO TO NEXT ;
  J = CELLJCCJ ; WRITE (POUT, F$AGE, F$ORAGE) END ;

```

END;

NEXT: DTNH1*0.6*TLIMB;
IF (DTNH1/DELTA-1.1)>0 THEN DTNH1*1.1*DELTA;
IF DTNH1>DTMX THEN DTNH1=DTMX;
DTN=DELTA; DELTA=DTNH1; UELTI=DTN+DELTA; GO TO LEFT;
ENQI.
FINISH: END.

APPENDIX II

MATERIAL DESIGNATIONS AND SUPPLIERS

<u>Designation in Text</u>	<u>Type and Supplier</u>
Aluminum Powders:	
Chunk	MD801 Oversize Aluminum Powder. Metals Disintegrating Corp. Elizabeth, New Jersey also Atomized Grade 40 Aluminum Powder. Reynolds Metals Co. Louisville, Kentucky
Spherical	No. H-322 Aluminum Powder Valley Metallurgical Co. Essex, Connecticut
Milled	No. A-547 Granular Ball-Milled Aluminum Powder. Fisher Scientific Co. Fairlawn, New Jersey
Flake	3xD Aluminum Powder Reynolds Metals Co. Louisville, Kentucky
MD-AK Aluminum Foam	MD-AK Aluminum Foam Emerson and Cuming, Inc. Canton, Massachusetts
Graphite and Carbon	All material supplied by National Carbon Company and referred to in text by manufacturer's designa- tions.
Silica Microballoons	Eccospheres SI Emerson and Cuming, Inc. Canton, Massachusetts

AFWL-TR-66-13

This page intentionally left blank.

APPENDIX III

TABULATED SUMMARY OF STATIC AND DYNAMIC DATA

AFWL-TR-66-13

This page intentionally left blank.

Table V
MEASURED LONGITUDINAL ACOUSTIC VELOCITIES

Type	Aluminum			Graphite and Carbon			
	Particle Size (μ)	Density (% g/cm ³)	Acoustic Velocity ^a (mm/ μ sec)	Type	Orientation	Density (% g/cm ³)	Acoustic Velocity (mm/ μ sec)
Chunk	149-120	2.38	4.89	ATJ	1	1.72	2.56
	149-120	2.10	3.16	ATJ	2	1.72	2.00
	149-120	1.38	2.31	ATJ	3	1.72	2.56
Milled	280-840	1.25	2.10	Grade 60	1	1.02	1.20
	280-840	2.10	3.85	Grade 60	2	1.02	1.41
	280-840	1.77	0.61	Grade 60 GA Colln	3	1.02	1.33
Flake	44-82	1.77	0.61	GA Colln	2	1.81	2.76
Spherical	5-106	1.73	3.83	CFA	3	1.00	1.70
Spherical	5-106	2.09	3.86	CEJ	2	0.94	1.21
Spherical + Microballoons	44-106	1.08	2.84	ACSR	2	1.55	1.85
XD-AH	100-1000 ^b	1.45	4.24				
Solid		2.77	6.27				

^a All measurements made at room temperature.

^b Pore size rather than particle size.

Table VI
SUMMARY OF GRAPHITE AND CARBON DATA FROM QUARTZ GAGE SKITS

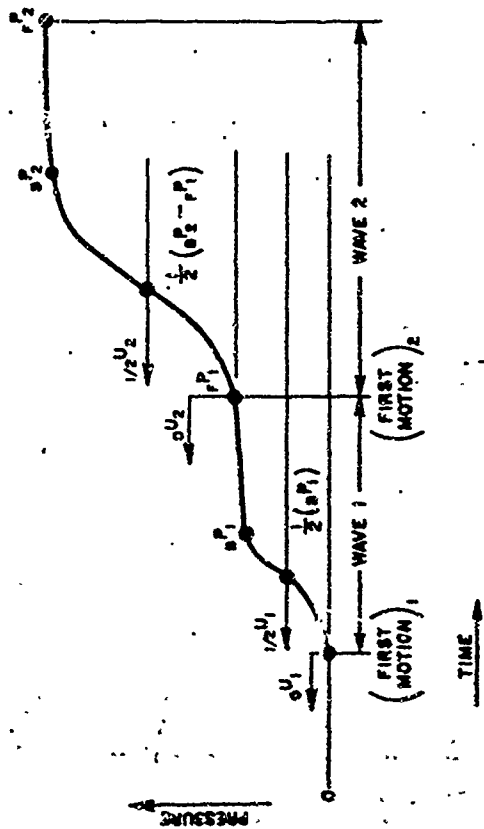
DESCRIPTION OF SPECIMEN		IMPACT CONDITIONS			WAVE 1 ^a		WAVE 2 ^b		CALCULATED MEGACROT DATA			
Type	Face Size (sq in)	Density (g/cm ³)	Thickness (cm)	SPMG NO.	Projectile Velocity (mi/sec)	Sketch Tilt Across Gage (degrees)	Velocity (mi/sec)	Pressure Skating in Quartz (lb/in ²)	Velocity (mi/sec)	Pressure Skating in Quartz (lb/in ²)	Pressure (lb/in ²)	Particle Velocity (mi/sec)
Carbon												
CFR-20(2)	140	1.00	2.54	11,316	0.217	--	0.685	0.079	0.55	--	1.10	0.210
CA Coke (2)	--	1.61	2.72	11,318	0.212	0.015	--	--	1.60	~ 7.6	4.65	0.182
Graphite												
CLS 20(2)	140	0.94	2.66	11,317	0.215	0.049	--	--	0.381	5.00	0.7	0.210
ASMR (2)	--	1.56	2.57	11,314	0.215	--	0.832	0.174	0.624	9.00	1.82	0.202
Grade 60 (2)	30	1.01	2.58	11,215 ^c	0.214	-0.210	--	0.13	--	~ 1.6	--	--
Grade 60 (3)	30	1.01	2.79	11,221	0.220	0.022	--	< 0.10	0.80	4.40	1.70	0.209
Grade 60 (2)	30	1.01	2.66	11,271	0.205	0.026	--	--	0.76	13.45	2.08	0.291
Grade 60 (3)	30	1.02	2.69	11,313	0.430	< 0.010	--	< 0.27	~ 7.86	17.6	3.38	0.407
Grade 60 (1)	30	1.02	2.71	11,222	0.084	< 0.010	--	< 0.10	~ 1.1	> 9.	7.2	~ 0.626
Grade 60 (3)	30	1.03	2.59	11,229 ^c	0.21 ^c	0.151	--	0.10	--	4.15	--	--
ATJ (1)	--	1.72 ^d	2.74	11,185	0.217	< 0.057	--	0.37	0.72	7.45	2.55	0.200
ALJ (1)	--	1.72 ^d	2.71	11,196 ^c	0.450	< 0.010	--	0.38	< 1.7	--	--	--
ATJ (1)	--	1.72 ^d	2.72	11,792	0.703	0.014	--	--	2.08	40.7	20.1	0.571
ATJ (3)	--	1.70	2.70	11,187	0.268	0.023	--	0.40	0.99	~ 10.4	4.17	0.241
ATJ (1 or 3)	--	1.72 ^d	2.73	11,184	0.216	0.023	--	0.49	0.90	7.5	3.07	0.196
ATJ (1 or 3)	--	1.72 ^d	2.72	11,183 ^c	0.209	0.036	--	0.70	1.11	6.5	--	--
ATJ (1 or 3)	--	1.72 ^d	2.72	11,181 ^c	0.640	0.022	--	--	--	> 14	--	--
ATJ (1 or 3)	--	1.72 ^d	4.18	11,192	0.207	0.026	--	0.45	0.90	~ 5.	2.63	0.190
ATJ (2)	--	1.73	1.61	11,799	0.158	0.035	--	0.62	0.77	5.0	2.01	0.149
ATJ (2)	--	1.72	2.74	11,577	0.234	0.056	--	0.36	1.01	10.0	3.65	0.229
ATJ (2)	--	1.71	1.58	11,530 ^c	0.240	0.011	--	--	1.30(7)	10.4	--	--
ATJ (2)	--	1.73	4.13	11,529	0.300	< 0.010	--	0.28	~ 1.20	14.2	5.32	0.270
ATJ (2)	--	1.72 ^d	2.74	11,526	0.303	0.025	--	--	~ 1.15	13.1	4.92	0.272
ATJ (3)	--	1.74	2.67	11,528	0.630	< 0.010	--	--	~ 1.56	~ 22.4	9.65	0.376
ATJ (2)	--	1.74	2.71	11,531	0.630	< 0.010	--	--	1.87	~ 37.0	17.3	0.529
ATJ (2)	--	1.74	2.73	11,791	0.706	< 0.010	--	--	2.08	41.1	20.6	0.570

^a See wire diagram below

^b Based on calibration curve of Fig. 9. Actual pressures should be higher—see discussion in Section VI

^c Because data from these shots were less reliable, they were not used for plotting Megacrot.

^d Nominal values.



WAVE DIAGRAM FOR TABLE VI

Table VII
SUMMARY OF ALUMINUM DATA FROM QUARTZ GAGE SHOTS

DESCRIPTION OF SPECIMEN			SHOT NO.	IMPACT CONDITIONS			WAVE 1°		WAVE 2°		CALCULATED MICRINOT DATA	
Type	Particle Size (μ)	Density (g/cc)		Thickness (mm)	Projectile Velocity (mm/msec)	Shock Title Across Gage (μsec)	Velocity $\frac{W_1}{W_2}$ (mm/μsec)	Pressure Reading in Quartz (P ₁) (kbar)	Velocity $\frac{W_2}{W_1}$ (mm/μsec)	Pressure Reading in Quartz (P ₂) (kbar)	Pressure (kbar)	Particle Velocity (mm/μsec)
Chert	149-420	2.06	2.65	0.215	<0.010	~1.8	0.47	~0.7	5.5	--	--	
	149-420	2.07	3.07	0.215	0.028	1.60	0.4	0.89	10.3	3.70	0.191	
	149-420	2.07	3.22	0.450	0.011	3.07(?)	0.60	1.84(?)	~27	--	--	
	149-420	2.08	1.64	0.222	0.035	~1.7	1.10	0.87	11.6	3.77	0.198	
	149-420	2.09	5.99	0.217	0.026	1.97	0.20	0.89	9.0	3.70	0.193	
	149-420	2.09	3.11	0.356	0.022	--	--	1.29	20.8	8.20	0.302	
	149-420	2.09	4.56	0.710	<0.010	--	--	2.82	36.6	24.7	0.548	
	149-420	2.10	3.08	0.131	0.012	1.25	0.60	~0.9	2.6	--	--	
	149-420	2.10	4.62	0.220	--	--	0.32	--	8.15	--	--	
	149-420	2.10	3.16	0.495	0.011	1.96	0.4	1.58	31.8	13.6	0.405	
Solid (2024-T31)	149-420	2.08	3.05	0.213	0.084	2.50(?)	0.23	1.04(?)	11.0	--	--	
	210-250	2.14	3.00	0.222	0.026	1.38	0.59	0.89	11.3	3.92	0.197	
	5-420	2.14	2.79	0.227	0.026	1.73	0.43	0.90	10.9	3.91	0.201	
	(Solid)	2.77	12.33	0.207	0.014	6.86(?)	4.60	5.74(?)	14.5	--	--	
	(Solid)	2.77	12.34	0.213	0.024	6.86(?)	4.60	5.74(?)	14.9	--	--	
	(Solid)	1.45	1.93	0.230	0.029	6.11	4.82	4.62	17.4	17.1	0.126	
	100-1000 ^d	1.45	1.93	0.207	0.037	1.50	1.70	--	--	--	--	
	100-1000 ^d	1.45	4.62	0.217	0.011	3.07	1.40	--	--	--	--	
	100-1000 ^d	1.45	4.68	0.693	0.012	3.99	0.77	<1.54	>14	--	--	
	100-1000 ^d	1.45	1.93	0.729	0.100	2.01	2.37	<1.64	--	--	--	
Milled	250-840	1.08	3.53	0.258	0.041	--	0.0	0.395	3.36	0.90	0.212	

Table VII (Concluded)

DESCRIPTION OF SPECIMEN			SWET NO.	IMPACT CONDITIONS			WAVE 1 ^c		WAVE 2 ^c			CALCULATED HUGHWOT DATA	
Type	Particle Size (μ)	Density (g/cm ³)		Thickness (mm)	Particle Velocity (m/sec)	Shock TISS Across Gap ^d (μsec)	Velocity (μm/μsec)	Pressure Reading in Quartz (μbar)	Velocity (μm/μsec)	Pressure Reading in Quartz (μbar)	Pressure (μbar)	Particle Velocity (cm/μsec)	
Spherical M-NYS	44-106	1.03	2.591	0.214	--	--	0.0	~0.39	3.05	0.80	0.208		
	5-106	1.74	2.73	0.217	--	1.70(17)	0.40	1.10(?)	12.03	--	--		
	30-106	3.08	3.55	0.212	--	--	(?)	0.52	6.51	3.40	0.19		
	62-74	0.14	2.27	0.220	--	--	0.41	--	--	--	--		
Spherical + Micro- Billions	44-106	1.35	1.65	0.213	--	--	0.0	--	5.7	--	--		
	44-106	1.53	2.87	0.207	0.034	0.621	0.123	0.532	4.25	1.70	0.196		
Flake	44-62	1.77	3.02	0.228	0.067	--	0.0	0.735	6.6	3.18	0.207		

^a See curve diagram following Table VI.

^b Based on calibration curve of Fig. 9. Actual pressures should be higher—see discussion in Section VI.

^c Reverse data from these shots were less reliable; they were not used for plotting Hugoniot.

^d Part size makes this particle size.

Table VIII
SUMMARY OF STATIC COMPRESSION DATA FOR CARBON AND GRAPHITE SPECIMENS

DESCRIPTION OF SPECIMEN			TEST CONDITIONS			TEST RESULTS			
Type ^c	Pore Size (m)	Density (g/cm ³)	Specimen Condition?	Maximum Pressure of Test (kbar)	Yield Stress (0.2% Offset) (kbar)	Elastic Modulus ^a (10 ¹¹ dyne/cm ²)	Compression $\Delta L/L$ at Maximum P (3)	Final Compression $\Delta L/L$ After Test (in die) (%)	
Carbon									
GA Coke (2)	--	1.554	Yes	--	0.913	103,000	--	--	
GA Coke (2)	--	1.554	Yes	3.327	--	--	18.3	6.09	
GA (2)	1.40	0.952	Yes	--	0.0301	67,000	--	--	
Graphite									
ATJ (1)	--	1.705	Yes	--	0.448	524,000	--	--	
ATJ (1)	--	1.665	No	--	0.396	439,000	--	--	
ATJ (1)	--	1.703	Yes	1.817	--	--	18.7	12.3	
ATJ (2)	--	1.708	Yes	--	0.382	323,000	--	--	
ATJ (2)	--	1.710	No	--	0.316	310,000	--	--	
ATJ (2)	--	1.698	Yes	1.817	--	--	19.5	1.61	
ATJ (2)	--	1.700	Yes	--	0.439	507,000	--	--	
ATJ (2)	--	1.690	No	--	0.492	334,000	--	--	
ATJ (3)	--	1.713	Yes	1.912	--	--	19.5	1.93	
Grade 60 (1)	30	1.02	Yes	1.041	0.057	80,300	48.0	26.4	
Grade 65 (3)	30	1.02	Yes	1.041	0.0553	80,300	47.2	35.8	
Grade 60 (1)	30	1.02	Yes	1.041	0.0642	97,800	46.9	34.2	
Grade 60 (1)	30	1.02	Yes	1.041	0.0615	93,000	52.3	37.0	
Grade 60 (2)	30	1.02	Yes	1.041	0.0456	114,000	48.4	36.5	
CEJ-Grade 20 (2)	140	0.930	Yes	--	0.018	31,300	--	--	
CEJ-Grade 20 (2)	140	0.930	Yes	1.817	--	--	55.5	45.1	
ASOR (2)	--	2.50	Yes	4.327	--	--	32.5	18.0	
ASOR (2)	--	1.50	Yes	1.041	0.159	204,000	25.0	7.03	

^a Numbers in parentheses indicate orientation.

Table IX
SUMMARY OF STATIC COMPRESSION DATA FOR ALUMINUM SPECIMENS

DESCRIPTION OF SPECIMENS			SPECIMEN NO.	TEST CONDITIONS		TEST RESULTS				
Type	Particle Size (μ)	Density (g/cm ³)		Specimen Slides Contacted?	Maximum P of Test (kbar)	Yield Stress (0.2% Offset) (kbar)	Plastic Modulus E (psi)	Compression ΔL/L at Maximum P (%)	Final Compression ΔL/L After Test (in die) (%)	
Aluminum										
Milled	250-840	1.03	Yes	--	0.0263	39,000	--	--	--	
Milled	250-840	1.03	Yes	1.817	--	--	59.4	57.9	--	
Milled	250-840	1.31	Yes	0.052	--	235,000	--	--	--	
Milled	250-840	1.31	Yes	1.817	0.106	--	40.2	40.2	--	
Milled	250-840	1.414	Yes	--	6.177	313,000	--	--	--	
Milled	250-840	1.402	Yes	1.817	--	--	63.9	42.9	--	
Milled	250-840	1.396	No	0.052	--	92,000	--	--	--	
Chunk	149-420	2.66	Yes	1.817	0.670	1,390,000	16.3	15.4	--	
Chunk	149-420	2.66	No	--	0.439	1,265,000	--	--	--	
Chunk	149-420	1.370	Yes	--	0.101	118,000	--	--	--	
Chunk	149-420	1.405	No	0.053	--	101,000	--	--	--	
Chunk	149-420	1.405	Yes	1.817	0.0970	223,000	44.5	40.0	--	
Chunk	230-420	1.994	Yes	--	0.0925	78,200	--	--	--	
Chunk	230-420	1.970	Yes	--	0.362	1,900,000	--	--	--	
Chunk	210-250	2.095	Yes	1.817	--	--	22.9	22.1	--	
Chunk	210-250	2.125	Yes	1.817	--	--	20.4	18.8	--	
Chunk	210-250	2.120	Yes	--	0.329	476,000	--	--	--	
Chunk	149-420	2.060	No	--	--	--	--	--	--	
Chunk	149-420	2.068	Yes	1.817	0.456	1,370,000	17.6	16.4	--	
Chunk	149-420	2.085	No	--	--	--	--	--	--	
Chunk	149-250	2.107	Yes	1.817	--	--	19.0	18.3	--	
Chunk	210-250	2.107	Yes	--	0.286	1,175,000	--	--	--	
Chunk	210-250	2.100	No	--	--	--	--	--	--	
Sph. micro	44-149	1.625	Yes	1.817	--	--	12.78	12.35	--	
Sph. micro	44-149	1.635	Yes	--	0.0923	456,000	--	--	--	
Sph. micro	44-149	1.635	No	--	--	--	--	--	--	
Sph. micro	44-149	1.110	Yes	1.817	--	--	54.7	54.0	--	
Sph. micro	44-149	1.100	Yes	--	0.0352	106,000	--	--	--	
Sph. micro	44-149	1.120	No	--	--	--	--	--	--	

Table IX (Continued)

DESCRIPTION OF SPECIMEN			SPECIMEN NO.	TEST CONDITIONS		TEST RESULTS			
Type	Particle Size (μ)	Density (g/cm ³)		Specimen Slides Confined?	Maximum P of Test (kbar)	Yield Stress (0.2% Offset) (kbar)	Elastic Modulus E (psi)	Compression $\Delta L/L$ at Maximum P (%)	Final Compression $\Delta L/L$ After Test (in die) (%)
Flake	37-62	1.787	Yes	0.053	--	--	10.05	1.10	
Flake	37-62	1.678	Yes	--	0.0011	4,250	--	--	
Spherical	5-106	2.110	No	--	--	--	--	--	
Spherical	5-106	2.105	Yes	1.817	--	--	17.7	17.9	
Spherical	5-106	2.100	Yes	--	0.215	1,425,000	--	--	
Spherical	44-62	2.125	Yes	1.817	--	--	16.6	16.6	
Spherical	44-62	2.130	Yes	--	0.176	933,000	--	--	
Spherical	44-62	2.125	No	--	--	--	--	--	

REFERENCES

1. Fowles, G.R. and D.R. Curran, AFSWC-TDR-62-22, 1962.
2. Rempel, J.R., AFWL-RTD-TDR-63-3056, 1963.
3. Rempel, J.R. and J. O. Erkman, AFWL-TR-64-119, 1965.
4. Al'tshuler, L.V., K. K. Krupnikov, B.N. Ledenev, V.I. Zhuchikhin, and M.I. Brazhnik, Sov. Phys. JETP 34, 606 (1958).
5. von Neumann, J. and R. D. Richtmyer, J. Appl. Phys. 21, 232 (1950).
6. Herrmann, W., E.A. Witmer, J.H. Percy, and A.H. Jones, ASD-TDR-62-399, 1962.
7. Wilkins, M.L., "Calculation of Elastic-Plastic Flow," in Methods in Computational Physics, Vol. 3, B. Alder, S. Fernbach, and M. Rotenberg, eds., Academic Press, New York, 1964, p. 211-253.
8. Wagner, M.H., W.F. Waldorf, Jr., and N.A. Louie, AFSWC-TDR-62-66, 1962.
9. Lundergan, C.D. and W. Herrmann, J. Appl. Phys. 34, 2046 (1963).
10. Erkman, J.O. and G.E. Duvall, "Elastoplasticity and the Attenuation of Shock Waves," paper presented at Ninth Midwestern Mechanics Conference (University of Wisconsin), August 1965 (Proceedings to be published).
11. Graham, R.A., T.W. Neilson, and W.B. Benedick, J. Appl. Phys. 36, 1775 (1965).
12. Al'tshuler, L.V., S.B. Korner, A.A. Bakanova, and R. T. Trunin, Sov. Phys. JETP 11, 573 (1960).
13. Doran, D.G., J. Appl. Phys. 34, 844 (1963).
14. Fowles, G.R., J. Appl. Phys. 32, 1475 (1961).
15. Lockyer, G.E., AFWL-TR-65-113, 1965.
16. Weast, R.C., S.M. Selby, and C.D. Hodgman (eds.), Handbook of Chemistry and Physics, 46th Ed., Chemical Rubber Publishing Co., Cleveland, Ohio, 1965.
17. Bernstein, D. and D. D. Keough, J. Appl. Phys. 35, 1471 (1964).
18. Williams, R., Stanford Research Institute, private communication: Manganin gage calibration (1966).